1-1-2014

The Investigation Of The Molecular Mechanism Of Rhodopsin Activation By Small Angle Neutron Scattering And Small Angle X-Ray Scattering Techniques

Kurt William Van Delinder

Wayne State University,

THE INVESTIGATION OF THE MOLECULAR MECHANISM OF RHODOPSIN ACTIVATION BY SMALL ANGLE NEUTRON SCATTERING AND SMALL ANGLE X-RAY SCATTERING TECHNIQUES

by

KURT WILLIAM VAN DELINDER

THESIS

Submitted to the Graduate School

of Wayne State University,

Detroit, Michigan

in partial fulfillment of the requirements

for the degree of

MASTER OF SCIENCE

2015

MAJOR: PHYSICS

Approved By:

_____

Advisor Date

DEDICATION

To the pursuit of knowledge and scientific advancement.

ACKNOWLEDGEMENTS

First and foremost, I would like to thank my advisor, professor Xiang-Qiang (Rosie) Chu whose expertise, understanding, and guidance have added greatly to my graduate school experience. Throughout the course of my studies, she has demonstrated by example what hard work, dedication and perseverance can accomplish in a fast moving, scientifically evolving world. I am indebted to her for allowing me to partake in so many extracurricular activities. The frequent experiments at Large National Laboratories, the many scientific conferences, and the opportunity to present at the University of Notre Dame have so far been the highlights of my entire academic career. My participation in these activities have served as a form of catalyst towards developing myself into an ambitious scientific professional and to that I thank you.

My sincere thanks must also go towards my fellow research group mates: Debsindhu Bhowmik, Utsab Shrestha, and Gurpreet Dhindsa. For the many hours spent together working on research projects, the open-minded sharing of knowledge and of course the camaraderie. I am grateful to have had such a pleasant and splendid group of colleagues to provide such a stimulating and fun environment to learn and grow.

Lastly, as my home away from home, I would like to thank my institution Wayne State University and the Physics Department for providing the setting, so that such scholarly activity can take place.

TABLE OF CONTENTS

LIST OF FIGURES

Chapter 1 – Introduction

1.1 – Introduction to Rhodopsin

1.1.1 - G-Protein Coupled Receptors (GPCR)

In 2012, a Nobel Prize in Chemistry was awarded to Robert J. Lefkowitz and Brian K. Kobilka for their scientific contributions made towards the study of G-Protein-Coupled Receptors (GPCR). As a result of their scientific endeavor, cellular biology has gained new ground with a newly discovered insight as to how cells relay messages. Specifically, they found out how it is that microscopic individual cells are able to make combined cellular movements as a response to a single applied stimulus. This fascination can be found and occurring to any distant location within a biological host.

We can now appreciate that the human body is a complex relaying network that depends upon the ability of many different types of cells to communicate messages effectively over long, mixed material distances. Each human cell is surfaced by an external membrane also called a phospholipid bilayer. The cellular membrane is used as a barrier to maintain separately the internal structures of a specific type of cell. However, information sent throughout the human body needs a way to transmit a signal to a specific cell so that an instruction to perform a function can be processed and executed upon request. The GPCRs serve as relay points to mediate the flow of outer cell information to the internal structures. They are positioned as composite gates found interjected within the cellular membrane. The name GPCR refers to a common mode of receptor signaling via GTP-binding proteins on the inside of the cell. Because their polypeptide chain passes seven times through the plasma membrane, the GPCRs are also called seven-transmembrane (7TM) receptors [1]. GPCRs are responsible for many different

biological conveyances such as: a change in concentration of peptides, hormones, lipids, neurotransmitters, ions, odorants, tastants or an influx of photons to the eye [1].

Mammalian GPCRs are usually grouped by amino acid sequence similarities into three distinct families A, B, and C. The International Union of Pharmacology Committee on Receptor Nomenclature and Drug Classification published reports on the nomenclature and pharmacology of GPCRs that consider their structure, pharmacology, and roles in physiology and pathology [2]. Rhodopsin has been investigated and studied since as early as the 1800s and although even today it is still not fully understood, there has been an extensive amount of biological, chemical and structural information collected as to classify it. On the basis of the predicted structure, conservation of few amino acids in the region critical for G protein activation, and activation by small ligand, rhodopsin belongs to the largest subfamily of GPCRs, family A [3].

1.1.2 - An Introduction to Rhodopsin

Rhodopsin is a visual pigment found within the rod photoreceptor cells of the retina. It is responsible for converting photons into chemical signals that stimulate biological processes in the nervous systems of humans and other vertebrate animals allowing them to sense light [4]. The vertebrate rod cell is comprised of an outer segment and an inner segment. The outer segment contains many stacks of disc membranes and within those disc membranes is the membrane protein Rhodopsin. In Figure 1.1 Rhodopsin is displayed interjected within the lipid bilayer.

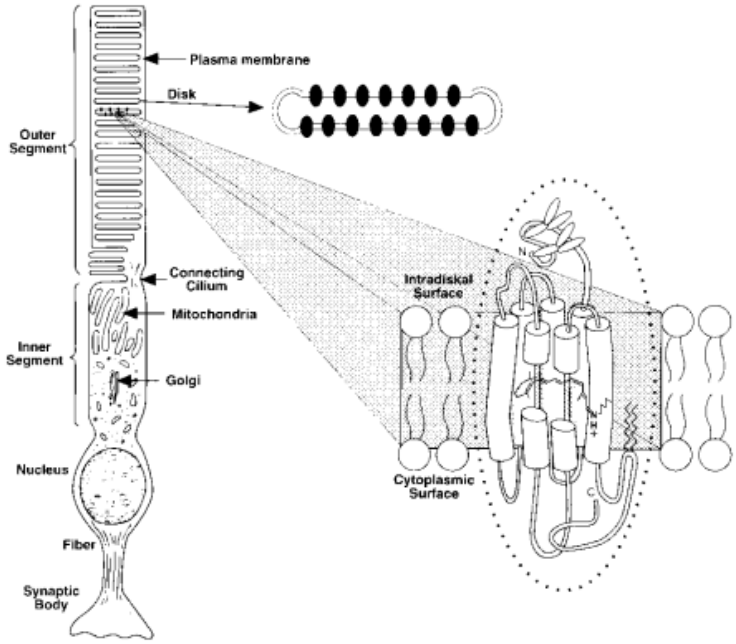

Fig 1.1 A structural image of a rod cell with a magnified image of a membrane disc. Rhodopsin can be seen within the phospholipid bilayer.

The process of how rhodopsin is activated is believed to be understood with the introduction of a large amount of intermediate states. When light exposure strikes a molecule of rhodopsin in a rod cell, a photon is absorbed, and as a result a structural change is found. The chromophore of rhodopsin is 11-cis-retinal; the sole function of light is to isomerize retinal from 11-cis to all-trans followed by a series of structural changes within the membrane. The nature of the changes at the molecular level is largely unknown due to a lack of knowledge of the three-dimensional structure of rhodopsin [5].

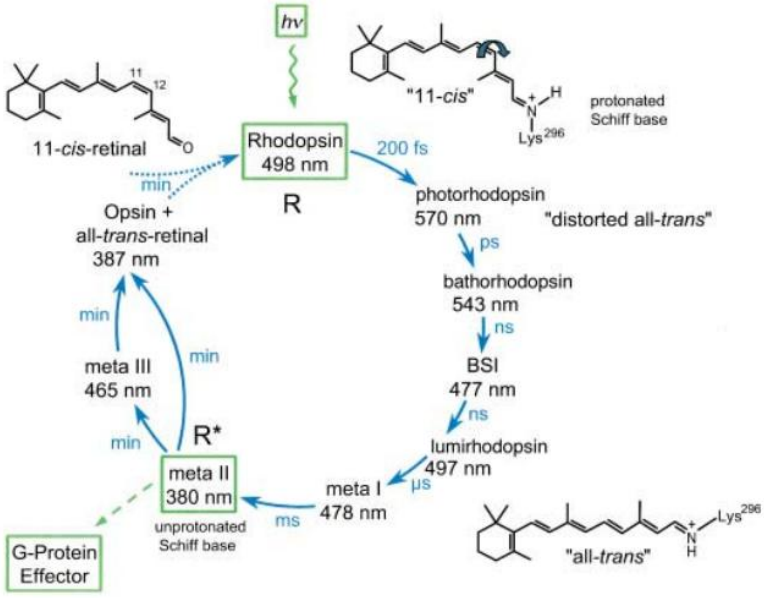

Fig 1.2 Photo-cycle of rhodopsin and photo-intermediate states.

1.1.3 - The Photo-intermediate States of Rhodopsin

In the dark, 11-cis retinal is bound by a protonated Shiff base linkage to the e-amino group of Lys^{296} in the case of bovine rhodopsin, which is stabilized by the carboxylate of Glu^{113} to form an intramembranous ion-pair [6]. Excitation of rhodopsin by photon absorption (approx. 500nm) isomerizes the 11-cis-ene to the trans form, which leads to the primary photo-product photorhodopsin within 200 femtoseconds [7]. The first high-energy intermediate of the relaxation process that can be stabilized at low temperature (-140^{o}C) is bathorhodopsin (λ max = 543nm). This intermediate stores two thirds of the photonic energy (~30kcal mol^{-}1) [8]. Thermal relaxation leads through a blue-shifted intermediate which does not accumulate at low temperatures and can only be obtained in time-resolved measurements to lumirhodopsin. In lumirhodopsin, which can be stabilized at -40^{o}C, most of the twist in the polyene chain has relaxed [9]. Metarhodopsin I (λ max = 478nm) and metarhodopsin II (λ max = 380nm) now follow and it is interesting to acknowledge a progressively longer decay time. A conformational change of rhodopsin is associated with the MI-MII transition, which exposes recognition sites on

the cytoplasmic domain for a signal transducing G protein known as transducin [6]. According to present knowledge the key triggering event in the visual process is the MI-MII transition of photolysed rhodopsin [10]. Finally the light-induced events result in decay of Meta II into opsin and all-trans-retinal by two parallel pathways, either directly or through Meta III, in which the Schiff base is protonated again [11].

Considerable knowledge has been obtained during the past 30 years concerning structure and function of rhodopsin and its orientation within the lipid bilayer. This has laid the groundwork for understanding how rhodopsin functions as a receptor of photons, how G-protein-coupled receptors may function generally, and how mutations in rhodopsin lead to a malfunctioning protein in diseases such as retinitis pigmentosa [12]. However, there are still major gaps in the understanding of the structural and dynamical basis for rhodopsin activation.

1.2 – Investigation of Rhodopsin using Small-Angle Neutron Scattering

Currently, X-ray crystal structures are available for rhodopsin in the dark state [13-15] as well as several freeze-trapped photo-intermediates, notably including a putative structure for Meta II [16, 17]. In addition rhodopsin has been extensively investigated by site-directed spin labeling [18] as well as solid state NMR methods [19]. Although conventional X-ray crystallography has played a prominent role in our understanding of rhodopsin activation, there are unanswered questions in the current model of rhodopsin activation. It is interesting to acknowledge an equilibrium in the photo-intermediate states of rhodopsin and the fact that each successive major intermediate has a lifetime order of magnitude greater than that which precedes it. There may be additional conformational sub-states present that are currently unknown.

With regards to the current model of rhodopsin, the key event that triggers the visual process is the formation of the Meta II state. The Meta I – Meta II transition involves a large

conformational change [18] that is connected with the activation of rhodopsin in the visual process. Lack of high-resolution dynamic structural information greatly impedes our progress in understanding the structural and dynamical basis for rhodopsin activation. Recently, two papers have been published that lead to exactly the opposite conclusions regarding the structural changes in rhodopsin that underlie activation of the Meta II form of rhodopsin [16, 17]. High-resolution structural information is lacking for the Meta I, and the Meta II structures are somewhat controversial [20].

The purpose of the experiment to investigate rhodopsin using a small angle neutron scattering technique is to firstly, observe the structural changes of the photo-intermediates of rhodopsin and secondly, to measure the effect of different detergents on the activation mechanism of rhodopsin. The results can be compared to a parallel investigation of the dynamic studies on conformational changes that will be conducted on human NSE protein.

The rhodopsin-detergent complexes are ideal systems to be studied by small angle neutron scattering (SANS) with contrast variation. Proteins and detergents, have inherently different scattering length densities, making contrast variation possible and enabling us to highlight individual components of a multi-component system without isotopic labeling of the sample. This can be achieved by varying the H_2O and D_2O (since hydrogen and deuterium also have significantly different scattering length densities) in the solvent. This approach allows us to isolate the structure of the protein and observe the influences of different detergents [21]. In addition, quantitative modeling of SANS data collected at specific contrast-matched points will allow the structural changes of rhodopsin in the visual process to be more fully understood.

1.3 – The Molecular Mechanism of Activation of Rhodopsin using Small Angle X-Ray Scattering (SAXS)

Synchrotron sources that produce x-ray scattering are one of the most powerful techniques used to study the structure and dynamics of proteins and almost all of the various assortments of biological samples. These sources extend from the radio-frequency to the x-ray regions of the electromagnetic spectrum, where the high wavelength x-ray side is termed the soft radiation and the short wavelength side as hard radiation since it penetrates the matter more easily. Thus, this technique is very useful to reveal the detailed information of the structure of the samples of the order of a few angstroms to the nanometer scale without damaging the sample immediately. These radiations are very intense and enable measurements to be conducted at faster speed and with better statistics. In addition, it is also a very useful technique in order to study the time resolved structure of the sample solution. As we are going to study the detergent-protein complex structure, SAXS technique suits very well for our different samples. We propose to study the structure of the detergent-rhodopsin complex where the detergents CHAPS and DDM stabilize the Meta-I and Meta-II photo-intermediates respectively when samples are activated by the light source. As this technique is very fast, we can study the time resolved structure of these complexes with superior statistics at sub-states Meta-I and Meta-II that exist only for several minutes before decaying.

The aim of this experiment is to use the small angle x-ray scattering (SAXS) technique to illuminate the structural changes of rhodopsin that lead to the activation of the photoreceptor, and thus triggering of the amplified visual response. Although X-ray crystallography has played a prominent role in understanding the structural details of rhodopsin activation, there are major gaps in our understanding of the large-scale changes in molecular shapes of the protein as it

occurs within a membrane environment. Structural changes in rhodopsin that follow 11-cis to trans isomerization of retinal will be investigated, including the time-ordered sequence of thermal relaxations that give the pre-activated Meta I state followed by the fully active Meta II state. Our aim is to unravel the mechanism of the multi-scale activation of rhodopsin and to establish the large scale structural changes for rhodopsin and its photo-intermediates near physiological temperature that underlie its activation. The issue of whether conformational changes of rhodopsin are on-off conformational switches or whether its activation involves an ensemble of states and sub-states will be explored through analysis of SAXS data during the photo-activated states. This experiment will illustrate the overall changes in shape and disposition of the trans-membrane helical elements that accompany the activation of visual processes.

Chapter 2 – Small Angle Neutron Scattering (SANS)

2.1 – An Introduction to Neutron Scattering

Typically, neutrons are able to penetrate matter to a far greater depth when compared to charged particles. Neutrons interact with atoms via nuclear rather than electrical forces, and nuclear forces are very short range – of the order of a few fermis (1 fermi = 10^{-15} meters). Thus, as far as the neutron is concerned, solid matter is not very dense because the size of a scattering center (nucleus) is typically 100,000 times smaller than the distance between such centers [23].

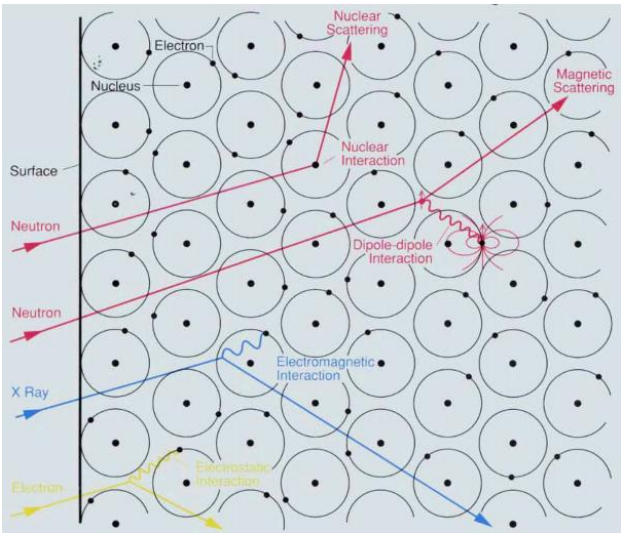

Fig 2.1. Scattering interactions by different methods.

Beams of neutrons, x-rays, and electrons interact with material by different mechanisms. X-rays and electron beams both interact with electrons in the material; with x-rays the interaction is electromagnetic, whereas with an electron beam it is electrostatic. Both of these interactions are strong, and neither type of beam penetrates matter very deep. Neutrons interact with atomic nuclei via the very short-range strong nuclear force and thus penetrates matter more deeply than either x-rays or electrons. If there are unpaired electrons in the material, neutrons may also interact by a second mechanism: a dipole-dipole interaction between the magnetic moment of the

neutron and the magnetic moment of the unpaired electron [23]. The ability of the neutron to penetrate deeply into a sample can be viewed as both a positive and negative attribute. The benefit is that the neutron has the ability to penetrate deeply into a sample even if it is in a container, which can be of great value for a liquid sample or if the sample has to be placed in a low temperature, high pressure setting. The downside is that the neutron even when scattered, appears to do so weakly in an interaction.

The scattering of a neutron by a single nucleus can be described in terms of a cross section σ, measured in barns (1 barn $=10^{-28}$ m^2), that is equivalent to the effective area presented by the nucleus to the passing neutron. If the neutron hits this area, it is scattered isotropically, with equal probability in any direction [25].

The incident neutron on a fixed nucleus can be represented by a wave function $\psi_i = e^{ikr}$, which is a plane wave expressed in terms of the unit vector r [25]. If the scattering nucleus is at the origin of the coordinate system, the wave function (represented by the circles spreading out from the nucleus in Fig. 2.2 of the scattered isotropic neutron waves can be written as, $\psi_s = -\frac{b}{r}e^{ikr}$ [25].

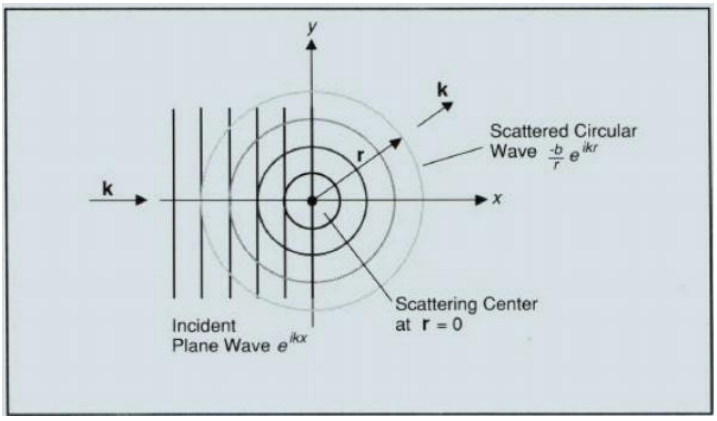

Fig 2.2 Neutron beam incident on a single scattering center.

The factor (1/r) takes care of the inverse square law that applies to all wave motions: the intensity of the neutron beam, given by the square amplitude of the wave function decreases as the inverse square of the distance from the source. The constant b is the 'scattering length' which represents the interaction between the neutron and scattering nucleus. The scattering length is related to the cross section by the equation $\sigma = 4\pi(b^2)$. The scattering length is a complex number, but the imaginary component only becomes important for nuclei with a high absorption coefficient (ex. Boron and Cadmium), otherwise it can be treated as a real quantity. The minus sign indicates that b is a positive number of repulsive interaction between the neutron and the nucleus [25].

Since neutron scattering is related to the nuclear scattering length, there is variation in size amongst each element in the periodic table. It also varies amongst isotopes of the same element. A commonly used example can be found in the comparison of ^{1}H and ^{2}H (hydrogen and deuterium). Hydrogen has a coherent scattering length of -3.74×10^{-5} Angstroms and deuterium 6.67×10^{-5} Angstroms [26].

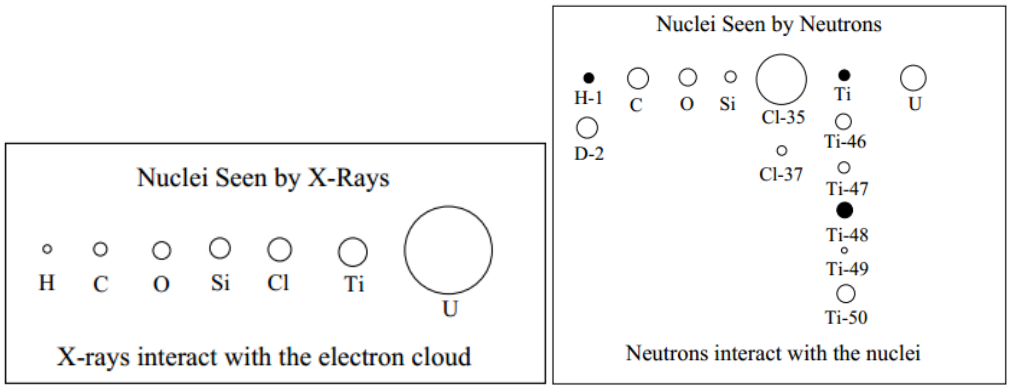

Fig 2.3 A comparison of neutrons scattered by nuclei to x-rays being scattered by electrons.

The neutron can also interact with the magnetic moment of an atom. This magnetic interaction has a separate magnetic scattering length that is independent from the nuclear

scattering length. It is possible to remove the nuclear component of the scattering and leave only the magnetic [26].

Previously, we looked at the case of the single nucleus, if we now consider a three dimensional assembly of nuclei still being scattered elastically, then the resulting scattered wave will then be,

$$\psi_s = -\sum \left(\frac{\mathrm{bi}}{\mathrm{r}}\right) \mathrm{e}^{\mathrm{ikr}} \mathrm{e}^{\mathrm{iqr}}$$

where q = ki – ks and is known as the scattering vector with ki and ks being the wavevectors of the incoming and scattered neutrons. The scattering vector shows the amount of momentum a neutron loses during a collision [25]. When |ki| = |ks|, it can be shown that $Q=4\pi\sin(\theta)/\lambda$ for elastic scattering.

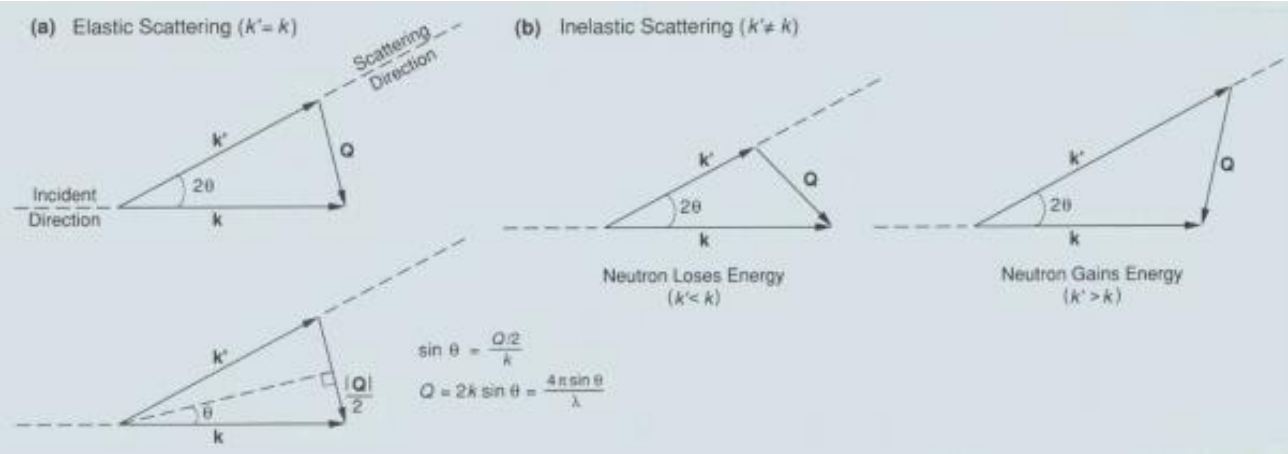

Fig 2.4 Scattering triangles for both a) Elastic and b) Inelastic.

The measurement of momentum transfer (Q) is one of two most fundamental quantities measured during neutron scattering. The second most fundamental quantity is a measurement of energy transfer defined:

$$\mathrm{h}\omega = \mathrm{Ei} - \mathrm{Ef} = \frac{\mathrm{h}^2}{2\mathrm{m}}(\mathrm{ki}^2 - \mathrm{kf}^2)$$

In such a case where the Energy is non-zero and the initial energy is greater than the final energy (Ei > Ef) or vice versa, this is referred to as inelastic scattering. In the situation where the final energy is equal to the initial energy this is referred to as elastic scattering.

Another important parameter in neutron scattering is the differential scattering cross section. In a neutron scattering experiment, where a beam of neutrons of a given E is incident on a general collection of atoms (your sample, crystal, polymer etc.), we can set up a neutron detector to count all the neutrons scattered. The solid angle dΩ is taken in the direction Θ,ϕ [26].

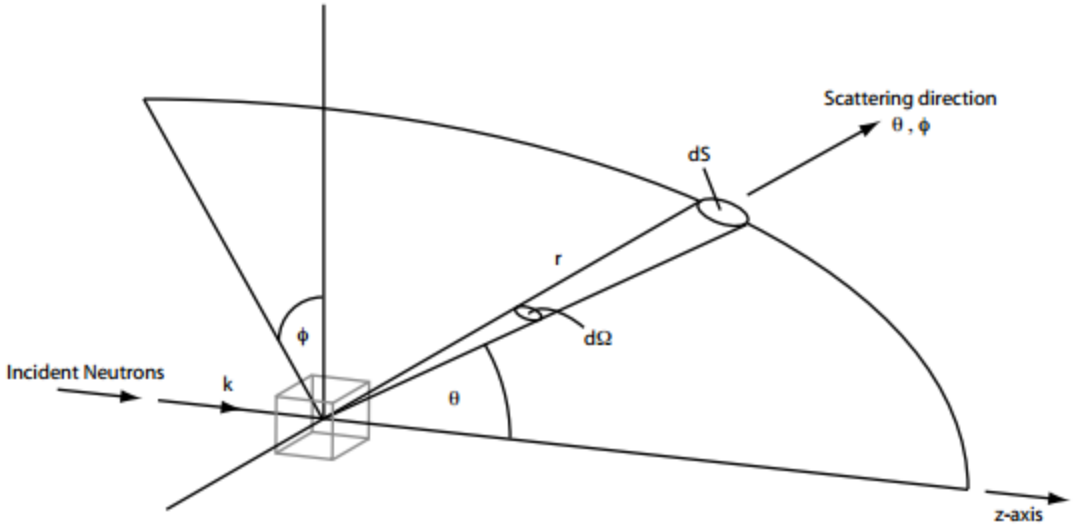

Fig 2.5 Geometry of a neutron scattering experiment.

The differential scattering cross section can be defined as:

$$\frac{d\sigma}{d\Omega} = \frac{\text{number of neutrons scattered per second into } d\Omega \text{ in direction } \theta, \varphi}{\varphi d\Omega}$$

Where ϕ is the number of incident neutrons per unit area per second or incident flux. The total scattering cross section is defined by the equation,

$$\sigma_s = \frac{\text{total number of neutrons scattered by second}}{\varphi}$$

This equation is directly related to the differential scattering cross section by,

$$\sigma_s = \int \frac{d\sigma}{d\Omega} d\Omega$$

The cross section is a quantity that is measured in a scattering experiment and derived by theoretical expressions that describe it for a given system of scatterers. Experimentally, cross sections are usually quoted per atom or per molecule and then the definitions above are then divided by the number of atoms or molecules in the scattering system [26].

We can calculate the differential scattering cross section from a single fixed nucleus assuming elastic scattering by manipulating the expressions above to reach new equations where the differential scattering cross section is equal to the scattering length squared and the total cross section can be related by,

$$\frac{d\sigma}{d\Omega} = b^2 \qquad \sigma_{total} = 4\pi r^2$$

Similarly, it is possible to calculate the differential cross section as a function of q for a collection of nuclei using some of the parameters in the resulting scattered wave equation listed above. The term b_i is defined as the incoherent scattering length.

$$\frac{d\sigma}{d\Omega}(q) = \frac{1}{N}\left|\sum_{i}^{N}(bi)e^{iqr}\right|^2$$

As mentioned previously, the scattering cross section is an interesting parameter and must be calculated by an expression depending upon the particular system of scattered nuclei. The simple derived equation for the differential scattering cross section is proportional to the scattering cross section and primarily was defined in an ideal scenario of one type of atom with zero spin and an elastic scattering interaction. However, real systems have a variety of both elements and isotopes of those elements. The total cross section is also going to be a combination of two components both a coherent and incoherent cross section.

Coherent scattering is when an incident neutron wave interacts with all the nuclei in a sample in a coordinated fashion. The scattered waves from all the nuclei have definitive relative phases and can interfere with each other [23]. The coherent scattering can be used to determine structural information.

Incoherent scattering is when an incident neutron wave interacts independently with each nucleus in the sample. The scattered waves from different nuclei have random relative phases and cannot interfere with each other [23]. No structural information can be obtained from incoherent scattering. The total cross section can be defined as,

$$\sigma_{tot} = \sigma_{coh+}\, \sigma_{incoh}$$

Both the incoherent and coherent cross sections are related to the mean of the variance of the scattering length.

$$\sigma_{coh} = 4\pi\langle b^2\rangle \quad \text{and} \quad \sigma_{incoh} = 4\pi(\langle b^2\rangle - \langle b\rangle^2)$$

As mentioned above, b the scattering length, can be a complex number. So, in the circumstance that the nuclei has a high absorption coefficient, we can add an additional cross section σ_a, which represents an absorption cross section. The total scattering cross section can now be defined as, $\sigma_{tot} = \sigma_{coh+}\, \sigma_{incoh} + \sigma_a$

Nucleus or isotope	σ_{coh} (10^{-24} cm^2)	σ_{incoh} (10^{-24} cm^2)	σ_{abs} (10^{-24} cm^2)
^{1}H	1.7568	80.26	0.3326
^{2}D	5.592	2.05	$5.19\ 10^{-4}$
^{3}He	4.42	1.6	5333
^{4}He	1.34	0	0

Fig 2.6 Distribution of coherent, incoherent, and absorption coefficients amongst various elements.

Notice that the coherent, incoherent and absorption scattering cross sections are significantly different between one particular element and vary largely between each differing element. As a result, it is possible to manipulate the elements within a sample in order to maximize the differences in scattering cross sections to single out the desired area that is being targeted by the neutron scattering experiment. This technique is most commonly called contrast matching.

There is an important structure factor S(Q, ω) which is useful because it can provide access to scattered data as a function of energy and momentum transfer. Defined as,

$$S(Q,\omega) = \frac{1}{2\pi}\int_{-\infty}^{\infty} I(Q,t)e^{(-i\omega t)}$$

Within the formula I(Q,t) is the intermediate scattering function defined as,

$$I(Q,t) = \frac{1}{N}\sum_{k,j}\langle e^{iQr_{k(t)}}e^{-iQr_j(0)}\rangle$$

Here rj and rk have to deal with the position of the particles at different times [27].

2.2 – Small Angle Neutron Scattering (SANS)

2.2.1 – Small Angle Neutron Scattering Technique

The aim of a small angle neutron scattering experiment is to determine the shape and the organization, averaged in time, of the particles or aggregates dispersed in a continuous medium. The term particle could mean many different objects, for example, small colloidal particles (clay, ferrofluid, nanotube), surfactant aggregates (micelles, lamellar, hexagonal, cubic, or sponge phases), polymers and all derivates, liquid crystal, model membranes, proteins in solution, flux line lattices in superconductors and many more [28].

Small angle scattering was discovered in the late 1930s by a physicist named Guinier during X-ray diffraction experiments on metal alloys [29]. The main principles and equations still used were exposed by Guinier and Fournet [30] in the very first monograph of a small angle x-ray experiment. SANS was developed approximately 30 years later in the 1960s. The increase of interest was related to the pioneering work of Sturhmann where contrast variation experiments demonstrated that neutrons were a powerful tool to investigate materials based on the variation of scattering length densities found within samples [28].

It is important to note that for small angle neutron scattering, often an elastic scattering technique is used to study structural details by measuring the intensity of scattered neutrons through a small angle usually from 0.2 degrees to 2 degrees. The formulas and techniques mentioned above for a fixed point like scattering are similar to the formulas used in small angle neutron scattering. One important piece of knowledge that should be paid special attention to before we get more into SANS formulae, is the fact that the scattering measurements are not performed in real space, like for example in a microscope. Scattering data is measured in a reciprocal or Fourier space. This means that in order to make use of our experimental data, we fit the reciprocal space data with fitting models that are well understood and we can then make determinations from the fitted data. This is a very important concept in dealing with SANS or any neutron scattering data.

An example to showcase the similarities of the previous equations with an increasing complexity of a sample scattered by SANS, is the consideration of a more realistic but still primitive scattering system of a sphere in a solvent. Previously, we were able to define the differential cross section of a fixed nucleus with the nucleus scattering length squared in a simple

relation. Now with a closer to realistic setting, we can define the coherent macroscopic scattering cross section as,

$$\frac{\mathrm{d}\sum_c(Q)}{\mathrm{d}\Omega} = \frac{\mathrm{N}}{\mathrm{V}} {V_p}^2 \Delta\rho^2 \mathrm{P(Q)S(Q)}$$

Where (N/V) is the number density of particles, Vp is the particle volume, $\Delta\rho^2$ is the contrast factor, P(Q) is the single particle form factor and S(Q) is the inter-particle structure factor.

S(Q) has a peak corresponding to the average particle inter-distance (the so-called coordination shell) in the case of a concentrated system where the particle inter-distance is of the same order as the particle size. The inter-distance is much larger than the particle size for a dilute system. The incoherent scattering cross section $d\Sigma i/d\Omega = \Sigma i/4\pi$ is a constant (Q-independent) background to be added to the coherent scattering level. Its contribution is mostly from hydrogen scattering in the sample [22].

An important concept used in neutron scattering and most certainly small angle neutron scattering is the ability to contrast match. Contrast matching is an isotopic-labelling technique based on the dramatic difference between the scattering lengths of hydrogen and deuterium, which is particularly useful in neutron-scattering studies of complex biological molecules in aqueous solution. This technique involves matching the scattering from the solvent with that from one component or both with deuterium. The observed scattering is then due to only the unmatched components [23].

2.2.2 – SANS Data Analysis

In order to understand SANS data, we create a number of standard plots that allow us to extract important information about our sample and experiment. These standard plots include

some variation of the term I(Q) (macroscopic scattering cross section $d\Sigma(Q)/d\Omega$) being plotted with some variation of Q (scattering variable).

2.2.2.1 – Guinier Analysis

The Guinier plot is graphed by plotting Ln[I(Q)] vs Q^2 (Ln refers to natural logarithm of I(Q)) in order to obtain the slope $Rg^2/3$ (Rg is the radius of gyration of the scattering objects). The expansion is as follows:

$$I(Q) = I_0 e^{\left(-\frac{Q^2 Rg^2}{3}\right)} \qquad Ln[I(Q)] = Ln[I_0] - \frac{Q^2 Rg^2}{3}$$

The radius of gyration represents the effective size of the scattering particle whether it is a polymer chain, part of a protein, a micelle, or a domain in a multiphase system. The usefulness of this plot stems from the fact that the obtained particle size, Rg is independent of the absolute intensity I_o and of any model. From the radius of gyration you can determine particular dimensions of different homogenous bodies [22]. For example: A sphere, ellipse, and a cylinder.

Sphere of Radius R: $Rg^2 = \frac{3}{5}R^2$

Ellipse with semi-axes a and b: $Rg^2 = \frac{a^2 + b^2}{4}$

Cylinder with radius R and length l: $Rg^2 = \frac{R^2}{2} + \frac{l^2}{12}$

It is interesting to note that the Guinier plot is modified when the scattering objects are elongated.

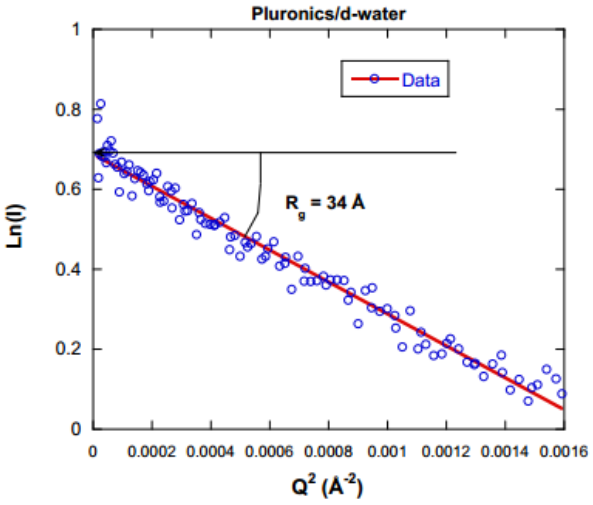

Fig 2.7 Example Guinier plot for SANS data from 10% (g/g) P85 Pluronic in D2O at 20°C. The slope is $Rg^{2/3}$.

2.2.2.2 – Porod Plot

The Porod region corresponds to a probed range smaller than the scattering objects so that the scattering radiation is probing the local structure. The Porod plot Log(I) vs Log(Q) (Log is base-10 logarithm) yields information about the so-called fractal dimension of the scattering objects [22]. At high-Q, one can approximate:

$$I(Q) = \frac{A}{Q^n} + B$$

A Porod slope n = 1 is obtained for scattering from rigid rods; a slope n = 4 represents a smooth surface for the scattering particle; whereas a slope n between 3 and 4 characterizes rough interfaces of fractal dimension D with n = 6 D. This is called a surface fractal. Moreover, in the case of polymer coils, the Porod slope n is related to the excluded volume parameter ν as its inverse n = 1/ν. A slope n = 2 is a signature of Gaussian chains in a dilute environment, a slope n = 5/3 is for fully swollen coils and a slope n = 3 is for collapsed polymer coils. A slope between 2 and 3 is for "mass fractals" such as branched systems (gels) or networks [22].

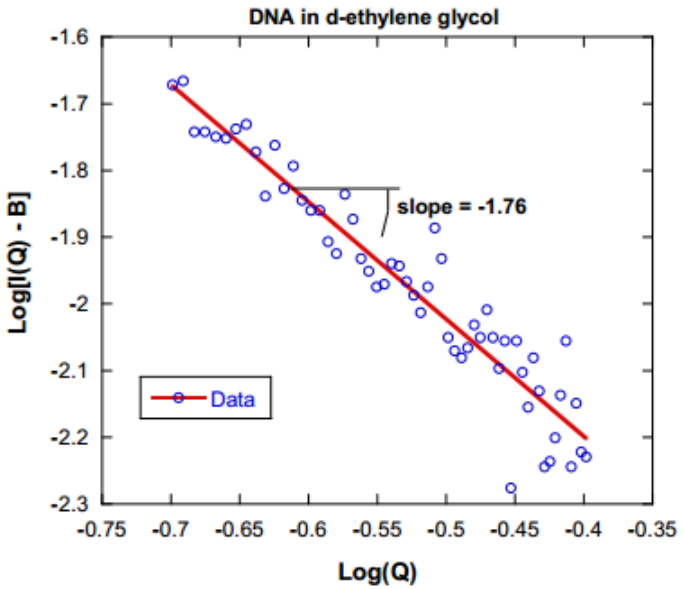

Fig 2.8 Example Porod plot for SANS data taken from 4 % (g/g) DNA coils in d-ethylene glycol at 50°C

2.3 - Investigating Rhodopsin by SANS Experiment

For the small angle neutron scattering experiment of rhodopsin, we have collected data from two samples: Meta I-CHAPS and Meta II-DDM. The photo-intermediates of rhodopsin are stabilized using different detergents, allowing the transitions between the specific states to be studied. The detergent CHAPS [31] can stabilize both the Meta I or Meta II states depending on the pH (~9 for Meta I and ~5 for Meta II), whilst DDM can stabilize the Meta II state regardless of pH [32].

For each sample, we acquire data for rhodopsin in the dark state and compare the effects of the different amphiphiles (detergent). Subsequently, each sample is exposed to light from a fiber optic cable to bleach the rhodopsin and initiate the transitions to the photo-intermediates. The Q-range is $0.01 < Q < 0.3$ Å^{-1} using 6 Å neutrons with a wavelength spread, $\Delta\lambda/\lambda$, of 0.15. This Q-range can be reached by using 1.1m and 6.8m detector-sample distances. The data for appropriate buffer solutions without protein is collected for use in the data reduction. Each sample measurement takes at least 4 hours, plus the background and resolution measurements.

2.4 - Materials & Methods

The detergent based samples are prepared by extracting rhodopsin from retinal disk membranes (RDM) from cattle retinas according to standard procedures in the Brown laboratory [19]. Purity is characterized by UV-is spectrophotometry with A280/A500 ratios of 2.2 indicating highly pure samples, and by SDS gel electrophoresis. Rhodopsin is extracted from purified RDM using DDM or CHAPS and purified by chromatography on Con-A sepharose [33]. Thus, the rhodopsin membrane reconstituted sample is prepared by extracting rhodopsin with dodecyltrimethylammonium bromide (DTAB) and the detergent exchanged by column chromatography on hydroxapatite. Proteolipid recombinant membranes are prepared by detergent dialysis. In order to keep all states stable, the samples were kept at 5 ˚C throughout the entire experiment.

Following experimental neutron scattering in the dark or photo-activated state, the samples are characterized by UV-visible spectrophotometry to determine the state of the Meta I/Meta II equilibrium. SANS data is collected at non-contrast matched points for rhodopsin/CHAPS complex (90% D_2O) and rhodopsin/DDM complex (80% D_2O). Data is also measured for contrast matched Rhodopsin/CHAPS complex at (19.8% D_2O).

The Biological Small-Angle Neutron Scattering (BioSANS) Instrument at the High Flux Isotope Reactor (HFIR), Oakridge National Laboratory (ORNL) is the scattering instrument used to study the various samples of rhodopsin used within this experiment. The wavelength for this instrument is from 6 to 25 Å and the wavelength resolution ($\Delta\lambda/\lambda$) = 9-45%. The capability for a range of sample-to-detector distance is from 1.1m to 15.3m. The detector installed is a 2-D Linear Position-Sensitive Detector and it has a resolution of 192x256 Pixels [34].

2.5 - Data Analysis

For this scattering experiment, the samples are prepared of the protein rhodopsin with a detergent, either CHAPS or DDM. For these particular samples, a standard model plot cannot really be used as an ideal tool to gain structural information about this type of complex. The rhodopsin-detergent complex is more sophisticated in shape and structure to be fitted by some variation of a simple shape to the experimental data. So, for this experiment we fit the data using a more advanced model called a necklace model or beads on a string model. This model is a form of a fractal model and assumes fractal-like aggregates built from spherical building blocks. In this model, the protein rhodopsin is randomly suspended in solution and takes the form of a long unfolded polypeptide chain with detergent like micelles randomly distributed along the length of it [35].

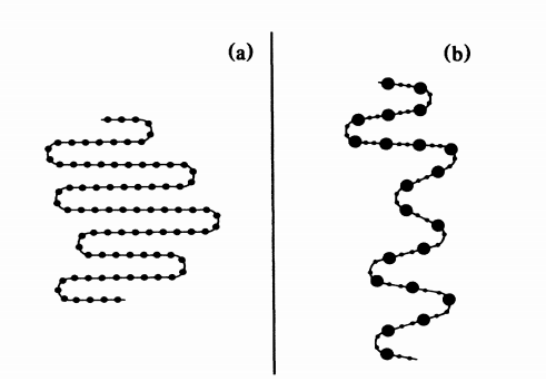

Fig 2.9 Schematic representation of the beads on a string model (a) native protein with small dots representing amino acids. (b) native protein denatured with large dots representing micelles and small dots still amino acids.

The scattering intensity distribution for a collection of micelle-like clusters along the unfolded polypeptide chain can be expressed as: [35]

$$I(Q) = \frac{N_l^2}{N_p N} {V_p}^2 (b_m - V_m \rho_s)^2 P(Q) S(Q) + B$$

N_1 and N_p are the number densities of the total surfactant and protein molecules in solution. V_m is the volume of the micelle and N is the number of such micelles attached to a polypeptide chain. b_m represents the scattering length of a surfactant molecule and ϱs is the scattering length density of the solvent. B represents the incoherent scattering background which is mainly due to hydrogen in the sample. P(Q) denotes the normalized particle structure factor of the micelle-like cluster. For a spherical particle of radius R, it is given by, [35]

$$P(Q) = \left[\frac{3\{\sin(QR) - (QR)\cos(QR)\}}{(QR)^3}\right]^2$$

S(Q) is the inter-particle structure factor that takes into account the inter-micelle positional correlations. In the fractal model, the arrangement of micelle-like clusters is assumed as fractal packing of spheres. For such a case, S(Q) may be written as, [36]

$$S(Q) = 1 + \frac{1}{(QR)^D}\frac{D\Gamma(D-1)}{[1+(Q\xi)^{-2}]^{\frac{D-1}{2}}}\sin[(D-1)\tan^{-1}(Q\xi)]$$

Where D is the fractal dimension of the micellar distribution in space and ξ the correlation length between particles that is a measure of the extent of unfolding of the polypeptide chain. R denotes the radius of micelles along the string [35].

2.6 - Results & Discussion

2.6.1 – Plot of rhodopsin/CHAPS complex without contrast matching.

Figure 2.10, is a plot comparing a complex of rhodopsin and the detergent CHAPS in both the dark state and the excited state. There is no use of the contrast matching technique for this sample. This means that the scattering scan observes the combined rhodopsin bound to the detergent micelle CHAPS in a complex form. The sample is at a high D_2O concentration, precisely 90%.

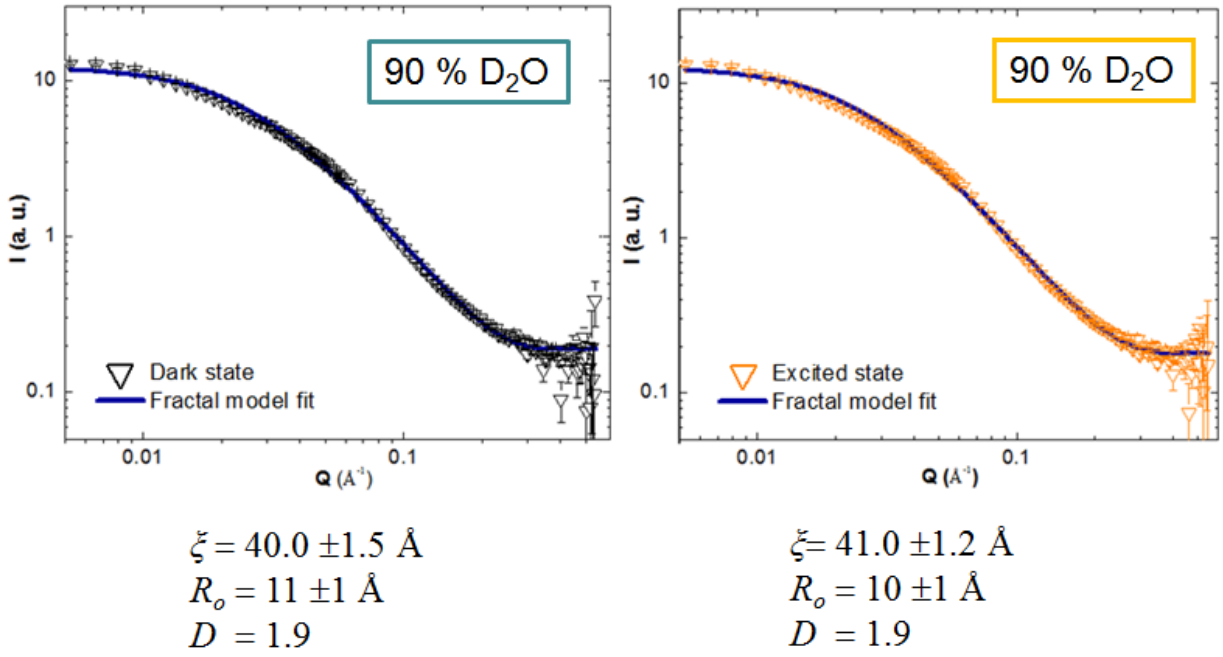

$\xi = 40.0 \pm 1.5$ Å
$R_o = 11 \pm 1$ Å
$D = 1.9$

$\xi = 41.0 \pm 1.2$ Å
$R_o = 10 \pm 1$ Å
$D = 1.9$

Fig 2.10 Plot of Intensity vs. Q for rhodopsin/CHAPS complex without contrast matching.

Between the dark state CHAPS-Rh plot and the excited state data plot, there appears to be little difference in the comparison of the two states. There is a small value change in the correlation length from 40.0 to 41.0 and of the radius of micelle from 11 to 10. This small numerical change is not a verification of a conformational change in structure from the dark state to a light state but, perhaps just an experimental difference that has occurred as a result of the neutron scattering. In the event of a conformational change the expectation would be for a far larger variation between the numerical values within the dark and excited state. Due to the fact that this data is not contrast matched, the rhodopsin/CHAPS detergent complex is being viewed. The likely cause of no observable structural change is because the detergent is surrounding the inner rhodopsin protein. Also, it has been proposed in previous data collection that CHAPS locks rhodopsin in the meta I state.

2.6.2 – Plot of rhodopsin/DDM complex without contrast matching.

Figure 2.11 is a plot comparing a complex of rhodopsin and the detergent DDM in both the dark state and the excited state. There is no use of the contrast matching technique for this sample. This implies that the scattering scan observes the combined rhodopsin/DDM complex. This sample is at a high D_2O concentration, 80%.

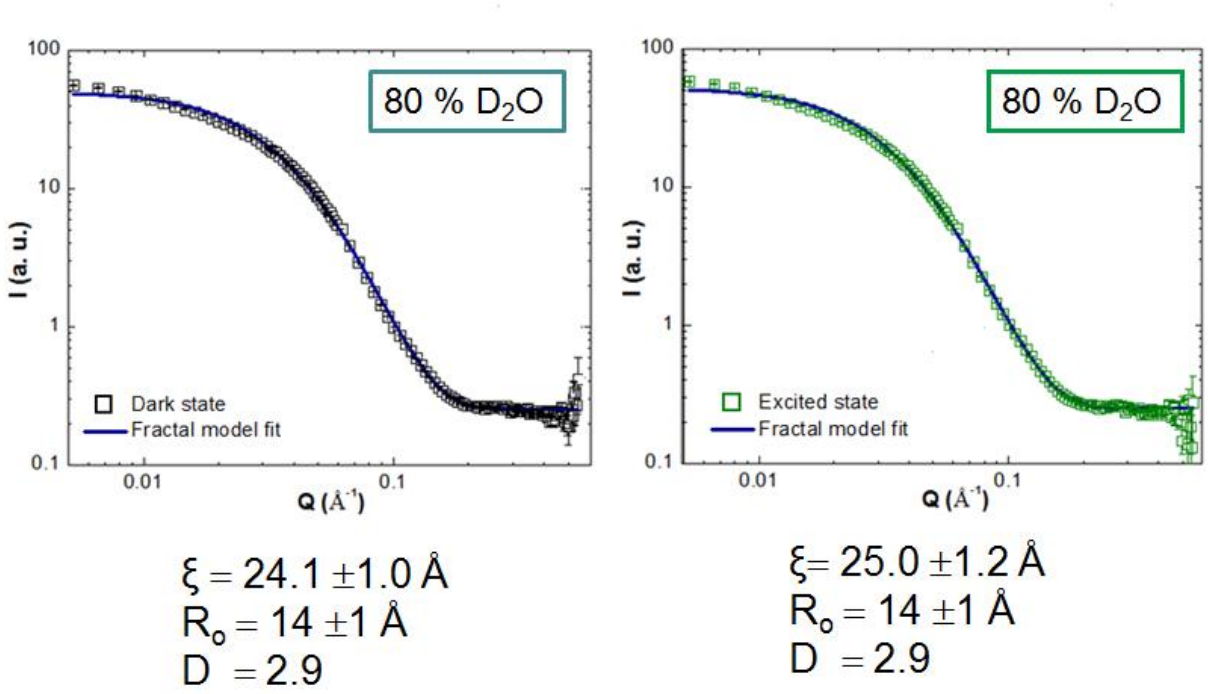

Fig 2.11 Plot of Intensity vs. Q for rhodopsin/DDM complex without contrast matching.

Similarly to the prior plot, there is little to no difference between the three parameters defining the structure of the rhodopsin detergent complex. There is still a slight change between the initial parameter values in the dark state and that in the excited state. Also, a change in the correlation length from 24.1 to 25.0. For the same reasons mentioned in Fig. 2.10, this slight value change does not necessarily conclude that there was a conformational change in structure. It is expected that there would be a far greater value discrepancy between the three parameters. It

has been proposed in previous scientific experimental papers that DDM locks rhodopsin into the Meta II state.

2.6.3 Plot comparison of rhodopsin/CHAPS and rhodopsin/DDM complex.

Figure 2.12 is a plot comparing rhodopsin-CHAPS and rhodopsin-DDM in an excited state. Both complexes are without the use of contrast matching. This figure is a comparison between the data collected from the excited state scans of the two prior plots.

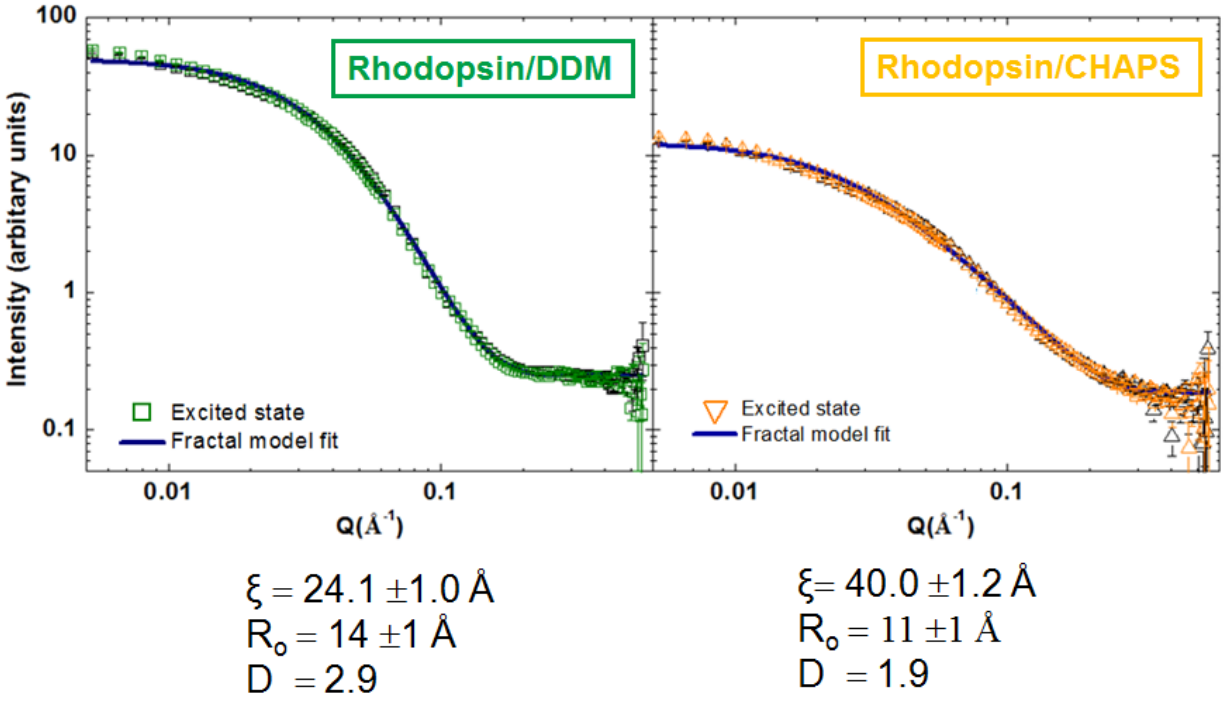

Fig 2.12 Plot comparison of rhodopsin/CHAPS complex and rhodopsin/DDM complex.

Comparing the two plots, it is interesting to notice the different values for each of the measured parameters. The correlation length being a measurement of the extent of unfolding is far greater in the rhodopsin/CHAPS complex, 40.0 to 24.1. The DDM detergent micelles are slightly larger than that used in CHAPS. The fractal dimension is larger in the rhodopsin/DDM complex as compared to that in the rhodopsin/CHAPS. When the measured fractal dimension is larger than the numerical value of another, it serves as a measureable proof of a less open

structure [37]. The Rhodopsin/CHAPS complex maintains a smaller fractal dimension which implies that it is a more compact structure. However, the correlation length in the Rhodopsin/CHAPS complex is much larger so by determination of parameter values the CHAPS micelles are in a more open structure.

2.6.4 Plot of rhodopsin/CHAPs complex contrast matched.

Figure 2.13 compares the complex of rhodopsin and the CHAPS detergent in the dark and excited state. This sample has been contrast matched and therefore means that the data collected in only from the protein rhodopsin structure. The D_2O concentration is 19.8%. For this data analysis, a simple guiner-porod model was used to fit the data. From this fitting, only a measurement of the radius of gyration is determined which can be used to make a simple approximation for the size and distribution of a given sample.

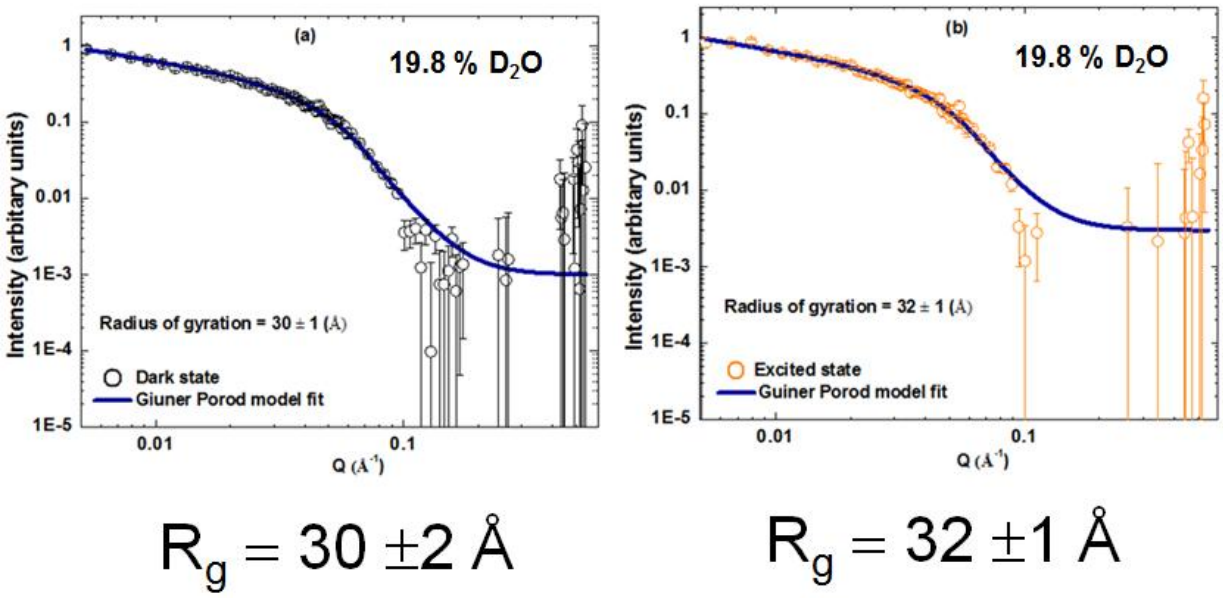

Fig 2.13 Plot of rhodopsin/CHAPs complex contrast matched.

It is interesting to note that although the data collected shows a slight change of the radius of gyration, both graphs are decisively the same. There isn't a true change in conformational structure that can be seen within the two data plots. However, it cannot be concluded that

rhodopsin does not change with the excitation of light but perhaps the change is masked by other experimental factors. One potential reason could be the fact that although the sample is contrast matched and is only the data collected from the protein rhodopsin. It is still technically in a complex form and most likely masked by the detergent CHAPS. Also, as previously mentioned there have been previous experimental insights mentioning that CHAPS is able to lock the protein into a Meta I state. Another possible reason could simply be that this instrument or scattering technique cannot properly detect the conformational change within the structure. This study should be continued perhaps with a scattering technique that has a greater resolution.

Chapter 3 – Small Angle X-Ray Scattering (SAXS)

3.1 – An Introduction to X-Ray Scattering

Contrary to neutrons, which are a particle, X-rays are a form of electromagnetic radiation. They have energies in the range of 100eV to 100keV, wavelengths in the range of 0.01 to 10 nanometers and frequency ranges from $3x10^{16}$ Hz to $3x^{19}$ Hz [38].

3.1.1 - X-Ray Interactions with Matter

X-ray interactions with matter occur by three different types of electromagnetic interactions: Coherent scattering, Compton scattering, and Photoelectric absorption.

Coherent scattering is when a low-energy incident photon passes near an outer electron of an atom. The incident photon ceases to exist and causes the electron to vibrate with the same frequency as the incoming photon. The vibration causes the electron to radiate a new x-ray photon with the same frequency and energy as the incident photon [39]. Coherent scattering only accounts for a small amount of photon interactions.

Compton scattering occurs when an incidental photon interacts with an outer orbital electron and receives energy to excite it so that it can be released from the atomic orbit. The incidental photon is then deflected from the atom and towards a new scattered direction [39]. The higher the energy of the incidental photon, the more likely the scattered photon will scatter in a forward direction. The probability of Compton scattering is directly proportional to the electron density of the material. The more electrons the greater the probability.

Photoelectric absorption occurs when an incidental photon no longer exists. The electron is ejected from its shell, and becomes a recoil electron. The electron hole becomes filled by an electron from a different shell and results in the release of a new characteristic photon [39]. Photoelectric absorption is directly related to the atomic number as a power of 3, Z^3.

It is interesting to note that in both Compton scattering and photoelectric absorption, an electron is produced which is then free to interact via two different processes: 1) collisional interactions which may result in the ionization or excitation of the affected atom. 2) radiation interactions which produce bremsstrahlung radiation. Secondary electrons eventually lose all their energy [39].

The probability of an X-ray beam to be absorbed is primarily dependent upon the energy of the beam and the thickness and atomic number of the material.

Due to the way that x-rays scatter, samples often require a substantially lesser amount to collect normal data from. As an approximation for a protein in solution, a sample volume usable for SAXS is 40 µl (exposed volume of 1-20 µl) while a volume much greater is necessary for SANS, 200 µl (exposed volume 150 µl) [40]. For sample proteins hard to find or expensive, this may be the difference of whether an experiment is possible or not.

3.1.2 X-Ray Sources

Since the probability of an X-ray beam being absorbed is dependent on energy, it is important to mention the different types of x-ray sources. There are many different varieties of X-ray sources but generally they can be grouped into three main categories: x-ray tubes, rotating anodes and synchrotrons. X-ray tubes and rotating anodes are commonly found and often a large university may have access to either of the two within their own facility. The basic design for an X-ray tube consists of a filament that acts as a cathode and can eject electrons. The electrons are capable of reaching high kinetic energy and collide into a metal anode to create x-rays. In the case of a rotating anode, the anode rotates to allow heat dissipation that can quickly over heat the system. Both the x-ray tube and rotating anode devices are designed to generate a fixed wavelength that is determined by the anode target material [41]. A synchrotron is a far more

sophisticated method to generate x-rays and can only be found at large scattering facilities. A synchrotron incorporates a cyclic like shape with the use of particle acceleration.

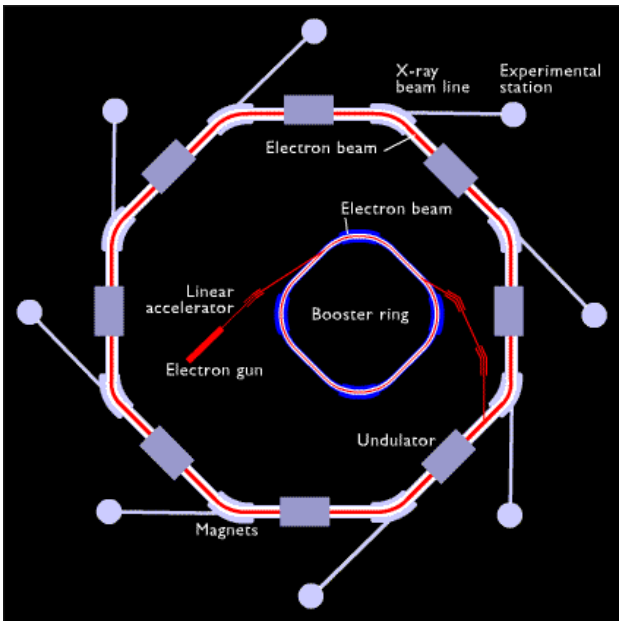

Fig 3.1 Example Diagram of a Synchrotron X-Ray Source.

Although synchrotrons can be used to accelerate a variety of charged particles, for this discussion we will focus on an electron. When an electron accelerates either by changing the magnitude or direction of its travel, it emits photons [42]. To accomplish this task there are two kinds of magnets, focusing and bending. The focusing magnets, which are quadrupoles, focus the electrons into a small beam. The bending magnets, which are dipoles, force the electrons to travel in a curved path [42]. As the electrons are accelerated by the bending magnet, they emit photons tangent to the curve along which they are travelling [42]. Usually the facility has accustomed the tangent photons to be within the energy of x-rays. At a synchrotron facility the user can vary the x-ray energy and pick the desired range for their particular sample.

3.1.3 – A Comparison of SAXS to SANS

It is interesting to note that SAXS shares the same basic scattering principles as SANS with the exception of a few small subtle differences. Both techniques are typically used to study structure and the interactions of systems generally of the size order of 10 to 1000 Angstroms. They also both tend to be used to view the same types of biological samples, such as, proteins, colloid, polymers and micelles and amphiphilic molecules [43]. In each technique radiation is scattered by a sample and the analysis on the resulting scattering pattern provides information about the size, shape, and correlations of the sample [43]. However, as mentioned in the neutron section and x-ray section, the scattering interaction that takes place between each technique are uniquely different. As a result of this difference almost every formula, data set and additional scattering information will have some variation between each technique.

Pointing out some of the key traits about SAX, it is important to note that x-ray scattering depending on whether the scattering involves lower range x-rays (soft) or higher range x-rays (hard) has a high throughput. Typically, it is the hard form of x-rays that are high in frequency and low in wavelength that hit the sample fast and can be used to collect information in a short-time scaled manner. For measuring biological phenomenon that appears only for a small duration of time, this trait is very important. High energy x-rays should still be used with caution because there is a potential to cause radiation damage to your sample and the risk increases with increasing energy. Radiation damage is far more unlikely with the use of a neutron source. Another interesting trait of using an x-ray modality is the ability to fine tune the beam to be micro-focused and even some facilities can achieve a nano-focused beam. This ability is employed with other x-ray techniques like scanning and diffraction [44].

	X-rays	Neutrons	Electrons
	$\lambda = \frac{hc}{E}$	$\lambda = \frac{h}{\sqrt{2m_n E}}$	$\lambda = \frac{h}{\sqrt{2m_e E}}$
Practical Units	$\lambda[\AA] = \frac{12.4}{E[keV]}$	$\lambda[\AA] = \frac{9.08}{\sqrt{E[meV]}}$	$\lambda[\AA] = \frac{12.3}{\sqrt{E[eV]}}$
Energy Range	1-100 keV	10-1000 meV	10-10^5 eV
Wavelength Range [Å]	10-0.1	3-0.3	4-0.04
Penetration Depth	1-100μm	1-50mm	1-100Å

Fig 3.2 Comparison of X-Ray, Neutron and Electrons Scattering Traits.

Found similar in both x-ray and neutron scattering experiments, the data pattern is collected in terms of the Intensity as a function of the amplitude of the scattering vector or momentum transfer (q). Q was fully introduced in section 2.1 and Intensity is defined for both x-ray and neutron scattering as follows:

$$\text{SANS:} \quad I_n[Q] = \frac{N_p}{V}\left|\int_{Vp} \Delta B_n[r] e^{[iQr]} d^3r\right|^2 S[Q] + I_{incoh}$$

$$\text{SAXS:} \quad I_x[Q] = \frac{N_p}{V}\left|\int_{Vp} \Delta B_x[r] e^{[iQr]} d^3r\right|^2 S[Q] + I_{bg}$$

Upon first glance it appears as though both I[Q] formulas are identical for both techniques but the term ΔB is correlated to the nuclear scattering length for neutron scattering and the electron density for x-ray scattering.

$$B(r) = \langle b_i \delta(r - r_i) \rangle$$

To make things clearer we can define a variable p(r) which is defined as,

$$\rho(r) = \langle b_i \delta(r - r_i) \rangle \qquad \rho = \frac{\sum_1^n b_i}{V}$$

Where $\rho(r)$ is the scattering length density and is directly related to the scattering length b_i, which was defined earlier and is the local interaction of radiations with materials.

Element	b^a_{coh} (10^{-12} cm)	σ^a_{inc} (10^{-24} cm^2)	$f_x(0)$ (10^{-12} cm)
Hydrogen	−0.3742	79.90	0.28
Deuterium	0.6674	2.04	0.28
Lithium-6 (7.5%)	0.201	0.41	0.84
Lithium-7 (92.5%)	−0.222	0.78	
Carbon	0.6648	0.001	1.69
Nitrogen	0.936	0.49	1.97
Oxygen	0.5805	0.0009	2.25
Fluorine	0.5654	0.0008	2.67
Sodium	0.363	1.62	3.09
Magnesium	0.5375	0.077	3.38
Phosphorus	0.513	0.006	4.23
Sulphur	0.2847	0.007	4.5
Chlorine	0.9579	5.2	4.8
Calcium	0.490	0.03	5.6

Fig 3.3 Chart Showing the Coherent Scattering Length (b_{coh}), the Incoherent Scattering Cross-Section (σ_{inc}) and f(o) the X-Ray Scattering Amplitude in the Forward Direction f(o).

Figure 3.3 shows a comprehensive list of many elements with the respective coherent scattering lengths, incoherent scattering cross sections and x-ray scattering amplitudes. Notice that the x-ray scattering amplitude increases with atomic number of course due to the rise in electrons. In comparison, notice that the coherent scattering length varies and does not show a correlation from one element to the next. The hydrogen and deuterium show a markedly large difference in coherent scattering length.

In each Intensity formula the parameter ΔB is used and therefore it would be fair to assume that $\Delta\rho(r)$ would be the quantity of interest used to calculate the intensity. The change in scattering length density is defined in a simple system of protein and solvent as $\rho_p(r)$ and $\rho_s(r)$. $\rho_p(r)$ can be approximated if the internal density fluctuations within a protein are small throughout the entire protein. Notice that the intensity is proportional to $(\Delta B)^2$, so it would be fair to say that the Intensity is proportional to the scattering length density squared.

$$I(q) \propto \Delta\rho^2$$

Suppose, we had such a situation where the $\Delta\rho(r)$, the change in scattering length density was the same for both the protein and the solvent, there would be no small angle scattering

distinction from the protein observed. There is often many situations where the internal density fluctuations are generally insignificant. Contrast variation experiments involving the systematic manipulation of protein and solvent scattering densities can be used to an advantage in studies of protein complexes [45].

X-rays interact with electron clouds surrounding each atom. Thus, the more electrons about an atom, the more likely it is that x-rays will be scattered. Proteins generally have similar elemental compositions and therefore two different proteins will usually have a similar x-ray scattering density, and there is no easy and benign way to manipulate the scattering density of the solvent [45]. Since x-rays interact with the electrons, the potential for interaction increases with atomic number. Therefore, the scattering distribution will show a disproportion towards the scattering of elements with a higher atomic number as compared to low. This means that elements often found in abundance like Hydrogen, Oxygen, and Carbon will be under-represented in the scattering pattern.

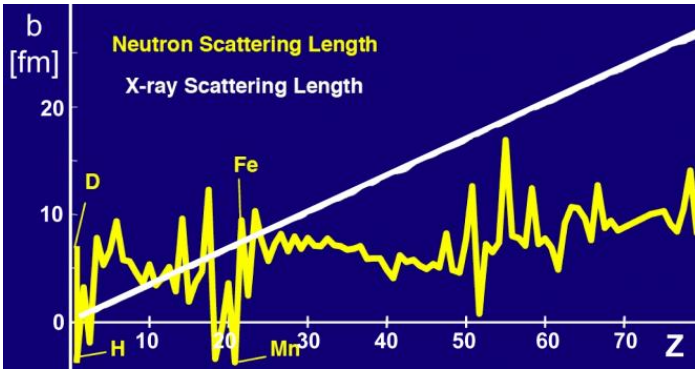

Fig 3.4 Graph Showing Comparison of Scattering Lengths for Neutrons and X-rays as a Function of Atomic Number.

Neutrons penetrate the electron cloud and are scattered by the atomic nuclei. The scattering powers of nuclei are determined by the properties of the neutron-nucleus interaction and vary in a non-systematic manner by atomic number and isotope [45].

As the data from an experimental scattering is collected in I(q) vs. (q), there is still a lack of structural information from this particular graph. I(q) vs (q) is in fact related to the shape of the macromolecule in solution but in order to make use of the scattering profile, it is useful to Fourier transform the scattering profile to obtain the inter-atomic distance distribution function, $\rho(r)$ [45].

In introducing the interatomic distance distribution function, it is interesting to acknowledge the difference in data both in a graph of $\rho(r)$and the original data I(q) vs (q) for the scattering of a protein solution using both techniques SAX and SANS.

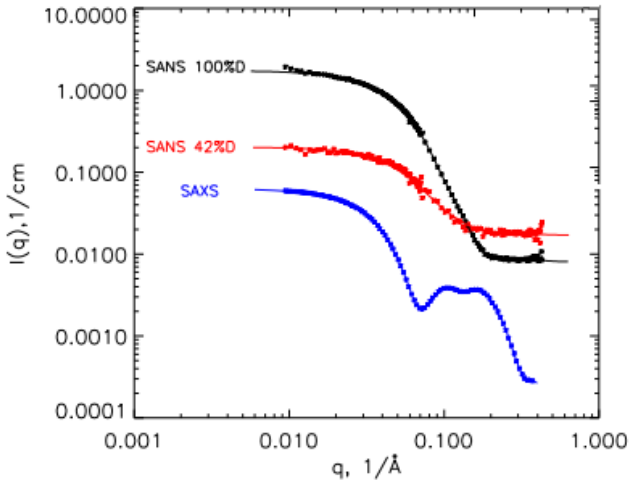

Fig 3.5 Plot of I(q) vs. q for a SAXS Scattering and SANS Scattering at Two Different Contrast Percentages of DLPC Nanodiscs.

Fig.3.5 is a plot of I(q) vs q for a sample solution DLPC Nanodiscs. The data collection is significantly different from SAX to SANS for a scattered sample. The flow of the curve is uniquely different at comparable q ranges. Notice from the q range from 0.060 to 0.100 that the collected SAXS data takes a steep dip in I(q) then actually climbs back up to create a valley like image in the graph. For this same q range and also the entire spectrum of measurement q, there is a smooth distribution of data for the SANS measurement and this trend is consistent for both the high percentage of deuterium and low percentage. The data collection for I(q) as a function of q

is markedly different for the same sample for both SAXS and SANS and even shows no real comparable consistency between the two.

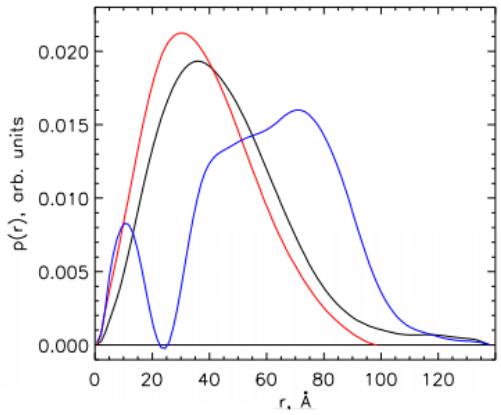

Fig 3.6 Plot of P(r) vs. r for a SAXS Scattering and SANS Scattering at Two Different Contrast Percentages of DLPC Nanodiscs.

Figure 3.6 is a plot of $\rho(r)$ vs r for the same sample in Fig. 3.5, which is of DLPC Nanodiscs. Blue designates the data collected from SAX, red from SANS at 42%D and the black is at 100%D. The $\rho(r)$ vs. r plot is a graph of the distance distribution function vs r which is the interatomic length. The $\rho(r)$ profile is sensitive to the symmetry and domain structure within proteins and as such can yield information concerning the shape and volume occupied by a protein or protein complex [45].

Similarly to the I(q) vs. (q) plot, the data shows no real comparability between the different scattering techniques. The two different contrasts in deuterium for SANS are somewhat similar but the SAXS data is not comparable at all. SANS is a smooth flowing single hill shape like data plot while the SAXS data shows peaks and valleys. This is interesting for a plot that is giving information about the structure of the scattered sample.

The conclusion to be made based upon both Fig.3.5 and Fig.3.6 plots is that there is not a direct comparison between experimental plots of data collection between SAXS and SANS for

the same sample. Data perhaps can be analyzed with some shared principles but, surely the formulas are not exactly the same for the two methods.

3.2 - Introduction to Scattering Data Processing

In section 2.2.2 SANS Data Analysis, two standard plots Guinier and Porod commonly used for data analyzing were explained giving the relevant mathematical formulas and an example plot to provide clarity to the application towards standard data. Since Guinier and Porod were already explained, they will only be briefly mentioned in this section describing the overall process of data analysis. Also, a software package called ATSAS which is comprised of a number of smaller individual softwares that are designed to accomplish the common tasks in data analysis will occasionally be mentioned in the following sections. The ATSAS software package is a popular choice for analyzing scattering data.

3.2.1 - Interpretation of Experimental Data

The experimental scattering of randomly oriented particles, background and other contributions result in an isotropic 1D pattern. This pattern is recorded on a 2D detector to improve the counting statistics of the scattering data [46]. The recorded pattern is normalized on an absolute scale and the intensity of the transmitted direct beam is measured. After scaling against the transmitted beam intensity and exposure time, the normalized 2D scattering pattern is transformed into a 1D array of scattering intensity I(q) as a function of q [46]. The scaling process is dependent on the detector type and beamline design. These steps are usually performed directly after the experimental scattering has taken place.

The scattering pattern of the solute is obtained by subtracting the scattering of the buffer measured separately from the scattered solution. There typically isn't much difference between the two patterns [46]. At smaller angles the signal is dominated from the background and at

larger angles due to the scattering from the solvent. Typically, both the buffer and sample are scattered in the same sample holder to avoid having to subtract the holder separately.

When scattering x-rays off of the sample, radiation damage is a potential problem, so often many exposures are taken of one sample so it would be easier to pinpoint.

Sometimes when a biological sample reaches a certain concentration, it can behave differently due to interparticle interference. Interparticle interference is a phenomenon where if there are too many particles close to each other, they can interact with each other via for example an electromagnetic force or another means. This can have direct consequences on the data collected in a scattering experiment. To correct for this, many samples are often prepared with various concentrations and the data can be merged or fused to eliminate any inconsistencies in data that has been collected. It is possible for interparticle interference to also influence the initial part of the scattering curve. To eliminate the influence one usually extrapolates to an infinite dilution, namely, having measured several samples with a difference in concentration assuming linear dependence of interference effects on concentration [46]. This can be done with repulsive interactions but works poorly for attractive interactions like aggregation. Aggregation can significantly influence the entire dataset making further processing impossible [46].

3.2.2 - Data Plots to Modelling

At this point several overall parameters can be evaluated by use of standard plots like the guinier plot, porod plot, and kratky plot. For the guinier plot, it is interesting to note that there are several software packages conveniently distributed, a popular one is AutoRG within the package ATSAS Primus [47]. The software is user friendly and allows you to pick freely the range for the guinier limits. The software comes with a feature to easily check the quality of data which would normally be determined by a kratky plot. A kratky plot is just a plot of $I(q)*q^2$ vs q and is a

common plot used to determine if a protein has been unfolded. The common sign is to observe a plateau over a specific range of q. If needed the porod plot can also be calculated within the ATSAS Primus package DATPOROD.

Now a distance distribution plot $\rho(r)$ can be calculated from the main features of shape and size of the solute particles, including Dmax [46]. Within ATSAS Primus, it can easily be determined in the software called GNOM by the simple one touch of a button.

3.2.2.1 - Ab Initio Modelling

From the scattering intensity pattern in 1D, we can reconstruct a 3D model of our samples shape. This reconstruction is termed ab initio modelling. The approach is often done in representing the particle as an ensemble of several thousand densely packed beads on a regular grid. Each bead belongs to either the particle (n=1) or to the solvent (n=0) so that the shape is described with a binary configuration [48].

Within the program ATSAS Primus there is a software commonly used called DAMMIN. Within the program they implement a bead modelling algorithm that also happens to be widely used in other programs. The algorithm is listed as follows,

$$\chi^2 = \frac{1}{N-1}\sum_{j=1}^{N}\left[\frac{I_{exp(sj)} - cI_{calc(sJ)}}{\sigma(sj)}\right]^2$$

The algorithm applies simulated annealing to build a compact interconnected configuration of beads that fits the experimental data by minimizing discrepancy between $I_{exp(s)}$ and a scattering profile computed from the model $I_{calc(s)}$ [48]. In the algorithm listed above c is the scaling factor, N is the number of points and θ denotes the experimental errors [48].

3.2.2.2 - Rigid Body Modelling

An additional way of modelling that is employed typically when there is a larger more complex macromolecule is called rigid body modelling. Rigid body modelling utilizes atomic models of individual subunits or domains deduced by high resolution methods to analyze the quaternary structure of a complex or multidomain protein in a solution [48]. The atomic building blocks are assumed to keep their tertiary structures upon formation of assembly. In this modelling, structural changes in response to external conditions as well as time-resolved studies are possible [48]. There are of course many other common modelling techniques.

3.3 - Investigating Rhodopsin by SAXS Experiment

For the small angle x-ray scattering experiment of rhodopsin, data was collected from three rhodopsin complex samples. Two of the samples are rhodopsin-detergent complexes, Rh-CHAPS and Rh-DDM, and one is a rhodopsin-member lipid complex, Rh-POPC. The Rh-CHAPS sample consists of a rhodopsin sample that is locked into the Meta I photo-intermediate state. The Rh-DDM sample has a Meta II photo-intermediate state in place for the rhodopsin sample. The detergent CHAPS can stabilize either the Meta I or Meta II states depending on the pH (~ 9 for Meta I and ~5 for Meta II), whilst DDM can stabilize the Meta II regardless of pH [49]. POPC isolates the Meta I and Meta II states in a similar manner to CHAPS.

For this experiment, we measure the samples at small and wide angles. The *Q* range is from 0.005 to 2 $Å^{-1}$. The data for appropriate buffer solutions without protein is also collected for use in the data reduction. So, we have three different complex samples and three buffer solutions to measure, including before and after exposure to light. Also, the samples are prepared for Rh-CHAPS and Rh-DDM in a different range of concentrations of detergent to protein ratios. For Rh-DDM the different molecular ratios are: 1:80, 1:123, 1:150, 1:200, and 1:400. For Rh-

CHAPS the different molecular ratios are: 1:50, 1:143, 1:226, 1:261, and 1:452. The ability for X-Ray scattering scans to be completed in a short amount of duration make this large amount of samples possible.

3.4 - Materials & Methods

The detergent based samples are prepared by extracting rhodopsin from retinal disk membranes (RDM) from bovine retinas according to standard procedures in the Brown laboratory [19]. Purity is characterized by UV-is spectrophotometry with A_{280}/A_{500} ratios of 2.2 indicating highly pure samples, and by SDS gel electrophoresis. Rhodopsin is extracted from purified RDM using DDM or CHAPS and purified by chromatography on Con-A Sepharose [33]. To keep all states stable, samples are kept at 5^{o}C throughout the duration of the experiment. Each sample complex was scattered using the small angle x-ray scattering technique while in dark state and then was exposed to a light source and had a new x-ray scattering scan to collect data in both states.

3.5 - Data Analysis

The two main plots that are showcased in the results and discussion for the collected SAX experiments are of a standard plot of I(q) vs q but with all the different molecular ratios for Rh-DDM and Rh-CHAPS. From the intensity I(q) formula we can then calculate the parameters P(Q) and S(Q).

$$\mathrm{I(Q)} = \frac{N_p}{V}(V_p \Delta \mathrm{B})^2 \mathrm{P(Q)S(Q)}$$

Where P(Q) is the particle form factor and determines particle size and shape of the intra-particle dimensions of the protein complex. S(Q) is the structure factor which gives inter-particle correlations of the protein complex. Between a graph comparing I(q) vs q for many samples, a

noticeable difference in data plots can be most likely attributed to a structural difference between samples. This determination is due to the fact of P(Q) and S(Q) being correlated to I(Q).

3.6 - Results & Discussion

3.6.1 - Plot of Rhodopsin-DDM complex with different molecular ratios

Figure 3.7, is a standard plot of comparing the different molecular ratios of rhodopsin and the DDM detergent. The Intensity range is from 1 to approximately 1000 and the q values range from about 0.01 to a little over 1.

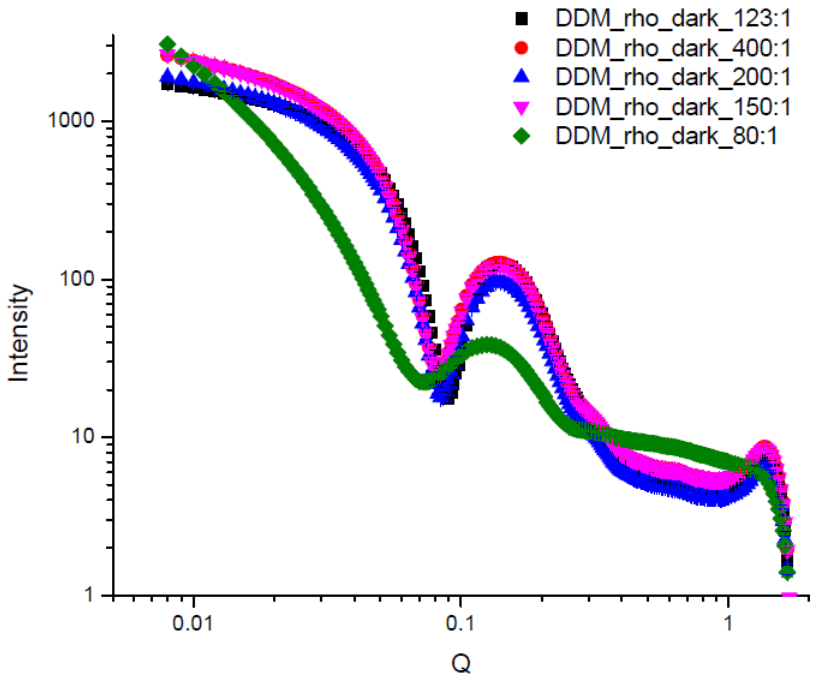

Fig 3.7 Plot of Rhodopsin-DDM complex with different molecular ratios.

Five different ratios of DDM to rhodopsin are displayed in this standard plot: 80:1, 123:1, 150:1, 200:1, and 400:1. There is little but still a notable difference in the intensity vs q plots between the 123:1, 150:1, 200:1, and 400:1 ratios. A small difference is going to be expected in the data with a change in molecular detergent to protein ratios. There is a greater separation between curves at the low q measurements and slight split from the medium to high. Generally, there is a trending shape in each of these plots which means that a similar model fitting could be

applied to these four plots with slight parameter changes. With the same model fitting being able to be applied, the shape of the complex is believed to be consistent amongst each data set.

The noteworthy protein-detergent ratio is the 80:1 DDM-Rh complex. The curve for this data set seems to show only a small collective coherence with the other graphed plots. The general trend of the plot seems to follow the same flow but the large difference in values in the I(q) vs q plot would transfer over to large structural differences. By the looks of the plots it may even be possible that the 80:1 DDM-Rh ratio may have a different model for fitting which means that it has a different complex shape. There is some notable change that takes place between the difference of 80:1 and 123:1. More data analysis procedures with the addition of advanced modelling should be used to investigate and give visual picture to this scientific occurrence. This may serve as preliminary data that could be used for a future experiment with molecular ratios between 80:1 and 123:1.

3.6.2 - Plot of Rhodopsin-CHAPS complex with different molecular ratios

Figure 3.8 compares Rhodopsin and CHAPS in complex form for many different molecular ratios. The intensity span is from 1 to 1000 and the q ranges from 0.01 to just over 1. There are five different ratios of Rhodopsin and CHAPS measured: 50:1, 143:1, 226:1, 261:1 and 452:1. For the protein-detergent ratios of 226:1, 261:1 and 452:1 there is a similar curve projection with slight increasing distance between plots with increasing ratio departure. The Rh-CHAPS ratios for 226:1 and 261:1 have very little separation while the 452:1 ratio shows some dissimilarity in distinguishable characteristics.

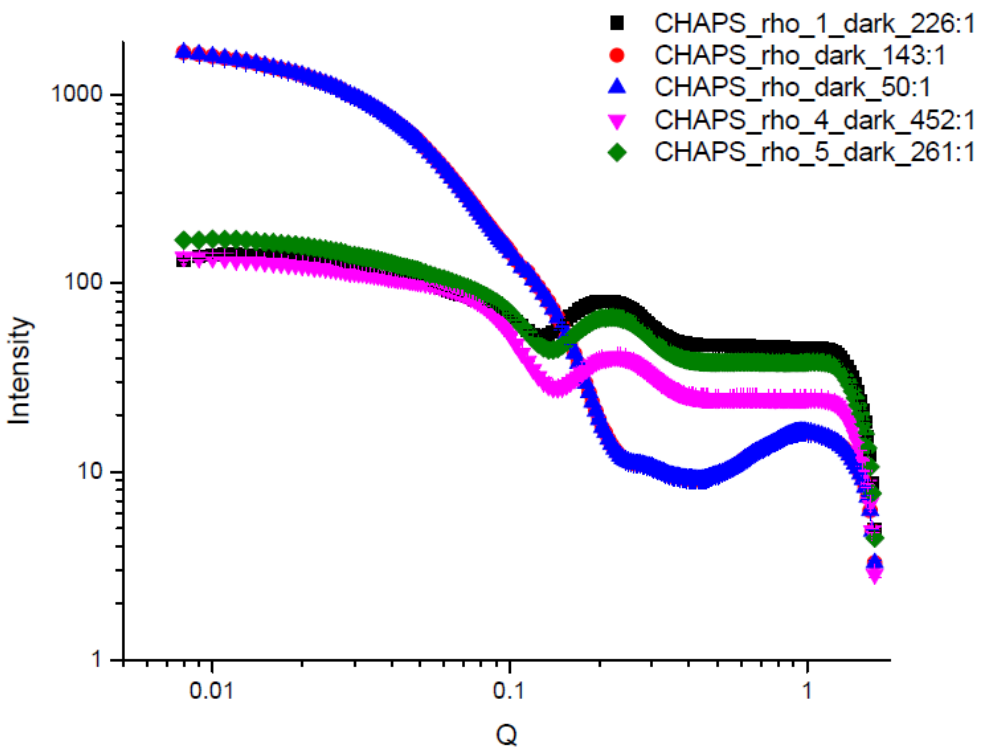

Fig 3.8 Plot of Rhodopsin-CHAPS complex with different molecular ratios.

Slightly different to the complex of Rh-DDM which had only one unsimilar ratio, two of the lowest ratios are uniquely different in plot trend from the other three ratios. Rh-CHAPS 50:1 and 143:1 shows no comparable tendency towards the other three molecular ratios. Due to the nature of the I(q) vs q plot, it would be fair to suspect that the Rh-CHAPS complex for 50:1 and 143:1 showcase a distinct structure complex different than the other ratios. A completion of greater data analysis should occur to investigate this phenomenon. Molecular modelling would be interesting to compare each of the molecular ratios.

Chapter 4 – Future Work

4.1 - Introduction to QENS

The technique of quasi-elastic neutron scattering (QENS) concerns itself with the measure of low-energy spectra associated with diffusive or vibrational atomic and molecular motion [50]. It is sensitive towards the pico-second to nano-second time scale from energies of 10^{4} to 10^{-2} μeV. Normally length scales are taken from a measurement of 1 to approximately 500 Angstroms and can cover both inter- and intra-molecular distances. Typically, a quasi-elastic neutron scattering event is measured using a time-of-flight (TOF) direct geometry, TOF indirect geometry 'backscattering', or a non-TOF indirect geometry [50].

BASIS is the name of a particular beamline at Oakridge National Laboratory in the Spallation Neutron Source facility. It utilizes a near-backscattering analyzer that incorporates a time-of-flight neutron scattering spectrometer. It can provide a very fine energy resolution, as low as 3.0 to 3.5μev at the elastic peak. The spectrometer is idealized for quasi-elastic neutron scattering that can provide a resolution of about 0.1% in energy transfers up to ~40meV [51]. The length and timescale of BASIS span from Angstroms and picoseconds to nanometers and nanoseconds are ideal for our biological study of rhodopsin [52, 53].

4.2 - Preliminary Results & Discussion

The preliminary data depicted is a collection of plots from three different samples using the BASIS scattering instrument. The three samples are of the detergent CHAPS, rhodopsin/CHAPS and opsin/CHAPS complex. Upon the photoactivation of rhodopsin, opsin is formed along with retinal and is reversed when rhodopsin is in the dark state. Due to the cyclical nature of the forming of opsin from rhodopsin, it is interesting to be able to compare the protein

dynamics between the two within a similar time scale. Another interesting component of the preliminary data is that the experimental samples were taken with a variation in temperature range from 220 Kelvin to 300 Kelvin. The entire temperature range is not provided but just the plots for the temperatures of 200K, 270K, and 300K are displayed. A standard plot of I(Q,t) vs time(ps) allows the ability to directly compare the protein dynamics amongst each sample and temperature.

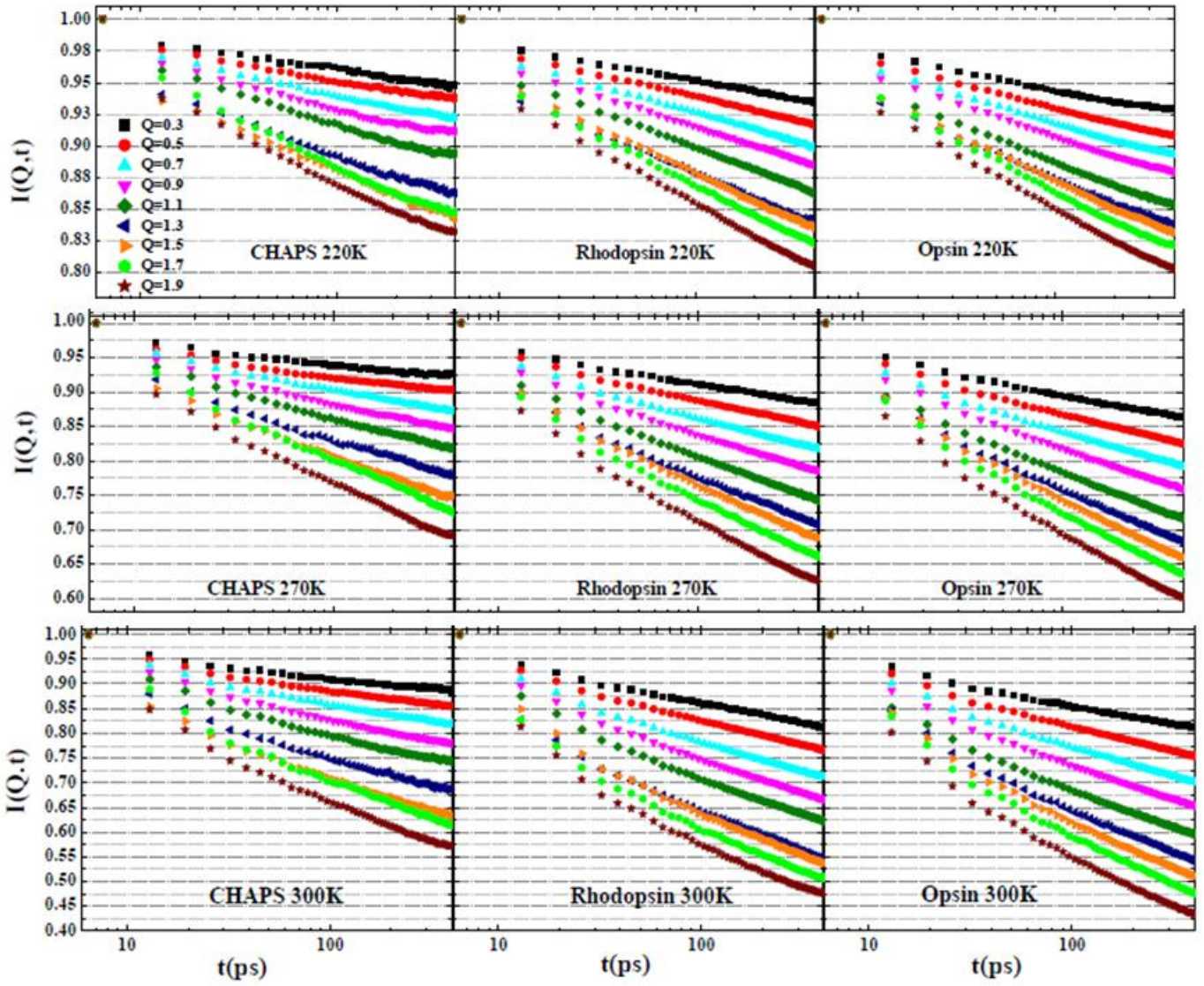

Fig 4.1 Plot of CHAPS, rhodopsin-CHAPS and opsin-CHAPS with experimental temperatures at 220K, 270K, and 300K.

Within figure 4.1, there is a consistent range along the x-axis from 10 to over 100 picoseconds. However, notice that the y-axis I(Q,t) tops off at the same measurement but begins at lower starting numerical values with increasing temperature.

At temperature 220K, there is a decreasing trend in I(Q,t) from CHAPS to rhodopsin to opsin. The decreasing I(Q,t) is found slightly with low q values and is found more prominent in measurements of higher q. The trend of decreasing I(Q,t) from CHAPS to rhodopsin to opsin can be seen for all three temperature plots. Overall as the temperature increases, the values for I(Q,t) become consistently lower for all three samples for both low q and high q values.

Chapter 5 – Conclusion

Due to the significant role that the G-Protein Coupled Receptor Rhodopsin plays within the light/dark visual process. It is important that we investigate the structure and dynamics of rhodopsin by scattering techniques to gain new scientific insight. For this thesis, three different scattering techniques in three different experiments and setups were employed to gain new valuable insight into the membrane protein.

Within the first experiment, small angle neutron, we were able to use rhodopsin in complex form to explore if we would be able to determine any structural change between rhodopsin samples in a dark state and upon photo-activation. Unfortunately, we did not see any notable parameter size changes. Also, within a contrast matched complex of CHAPS-Rh, there was no real standout change in structural values between a dark and photo-activated state. In comparing the two complexes of CHAPS-Rh and DDM-Rh there were clear parameter value distinctions that showcased a large complex size difference.

The second experiment, which was the use of a small angle x-ray scattering technique on two detergent complexes DDM-Rh and CHAPS-Rh showed interesting results. The DDM-Rh molecular ratio values 400:1, 200:1, 150:1 and 123:1 all followed the same trend in an intensity vs q plot. However, the smallest ratio 50:1 seemed to display a plot distinctly different from the other molecular ratios. Slightly different, the CHAPS-Rh molecular ratios, 452:1, 261:1 and 226:1 showed the same trend in plot but the two lowest ratios 50:1 and 143:1 had a distinctly different graph.

The third experiment compared the detergent CHAPS, CHAPS-rhodopsin and CHAPS-opsin by technique of quasielastic neutron scattering on the BASIS instrument. Different temperatures 220K, 270K, and 300K were measured in a I(Q,t) vs tau(ps) graph. In short

there were two overarching trends found within the samples. The first was a trend of increasing dynamic range from CHAPS to rhodopsin to opsin for all temperature scales. The second was a general increase in dynamic range with an increase in temperature.

Each scattering technique delivered interesting results with new determinations of information. Further analysis of experimental data should be the logical approach before reaching any experimental conclusion. Follow-up experiments could be used to create samples directly related to a hypothesis. Also, uses of computer modelling could be harnessed to clearly show the bases for a scientific reasoning.

REFERENCES

1. B. K. Kobilka and R. J. Lefkowitz, *Scientific Background on the Nobel Prize in Chemistry 2012, Studies of G - protein - Coupled Receptors,* The Royal Swedish Academy of Sciences. **15**, 1 (2012).
2. K. Palczewski, Annu. Rev. Biochem. **75**, 743 (2006).
3. T. Mirzadegan, G. Benko, S. Filipek, K. Palczewski. Biochemistry. **42**, 2759 (2003).
4. R. Hubbard, and A. Kropf, Proc. Natl. Acad. Sci. U.S.A.**44**, 130 (1958).
5. G.F.X. Schertler, C. Villa and R. Henderson, Nature **362**, 770 (1993).
6. M. F. Brown, Chemistry and Physics of Lipids **73**, 159 (1994).
7. R. W. Schoenlein, L. A. Peteanu, R. A. Mathies, C. V. Shank, Science **254**, 412 **(**1991).
8. A. Cooper, Nature **282**, 531 (1979).
9. U. M. Ganter, W. Gartner, and F. Siebert, Biochemistry **27**, 7480 (1988).
10. L. Stryer, J. Biol. Chem. **266**, 10711 (1991).
11. O. P. Ernst, and F. J. Bartl, Chem. Biochem. **3**, 968 (2002).
12. P. A. Hargrave, IOVS **42** (1), 3 (2001).
13. D. C. Teller *et al.*, Biochemistry **40**, 7761 (2001).
14. T. Okada *et al.*, J. Mol. Biol. **342**, 571 (2004).
15. J. Li *et al.*, J. Mol. Biol. **343**, 1409 (2004).
16. J. Standfuss *et al.*, Nature **471**, 656 (2011).
17. H. W. Choe *et al.*, Nature **471**, 651 (2011).
18. C. Altenbach *et al.*, Proc. Natl. Acad. Sci. U.S.A. **105**, 7439 (2008).
19. A. V. Struts, G. F. J. Salgado, and M. F. Brown, Proc. Natl. Acad. Sci. U.S.A. **108**, 8263 (2011).
20. E. Zaitseva, M. F. Brown, and R. Vogel, J. Am. Chem. Soc. **132**, 4815 (2010).
21. S. C. M. Teixeira *et al.*, Chem. Phys. **345**, 133 (2008).
22. B. Hammouda, *Probing Nanoscale Structures – The SANS Toolbox,* WWW Document, (http://www.ncnr.nist.gov/staff/hammouda/the_SANS_toolbox.pdf).
23. R. Pynn, *Neutron scattering: a primer*. Los Alamos Science, 1990. **19**: pp. 1-31.
24. S. Chawang, M.S. thesis, University of Oklahoma, 2010.

25. V. Lee, *Neutron Scattering Technique* (University of Oklahoma, Norman, OK, 2011), pp. 1-5.
26. A. J. Jackson, *Introduction to Small-Angle Neutron Scattering and Neutron Reflectometry* (NIST, Gaithersburg, MD, 2008), pp.1-18.
27. G. L. Squires, *Introduction to the theory of thermal neutron scattering*. (Cambridge University Press, Cambridge, 2012), pp. 1-20.
28. R. Borsalli, in *Soft Matter Characterization*, edited by R. Pecora (Springer, New York, 2008), Vol 2, pp. 705-761.
29. A. Guinier, Ann. Phys. Paris. **12**, 161 (1939).
30. A. Guinier, in *Small Angle Scattering of X-rays*, edited by G. Fournet (Wiley, New York, 1955).
31. S. Keita *et al.*, Biochemistry **49**, 736 (2010).
32. S. Arnis, and K. P. Hofmann, Proc. Natl. Acad. Sci. U.S.A. **90**, 7849 (1993).
33. W. J. De Grip, Meth. Enzymol. **81**, 197 (1982).
34. P. Langan, *The Biological Small-Angle Neutron Scattering Instrument at HFIR*, WWW Document, (http://neutrons.ornl.gov/biosans).
35. S. Chodankar, V.K. Aswal, P.A. Hassan, A.G. Wagh, *Physica B*, **398,** 112 (2007).
36. J. Teixeira, J. Appl. Crystallogr. **21**, 781 (1988).
37. S. H. Chen, Phys. Rev. Lett. **57** (20), 2583 (1986).
38. Materials Research Laboratory At UCSB, *X-ray Basics*, WWW Document, (http://www.mrl.ucsb.edu/centralfacilities/x-ray/basics).
39. M. Goaz and Pharoah, *Production of X-rays and Interactions of X-rays with Matter*, (Private Communication).
40. L. Arleth, *Combined use of SANS and SAXS*, WWW Document, (http://www.events.embo.org/13SAXS/presenter%27s_talks/Arleth_EMBO_SAS_Grenoble_May13.pdf).
41. B. Rupp, *An Introductory Course: X-Ray Sources*, WWW Document, (http://www.ruppweb.org/Xray/x-ray_sources.html).
42. P. C. Burnley, *Synchrotron Facilities*, WWW Document, (http://serc.carleton.edu/NAGTWorkshops/mineralogy/mineral_physics/synchrotron_facilities.html).

43. Zhang *et al*. J. Phys. Chem. B. **111** (250), (2007).
44. J. M. Carpenter, *Tenth National School on X-Ray and Neutron Scattering*, WWW Document, (www.dep.anl.gov).
45. D. A. Jacques, and J. Trewhella, Protein Science, **19**, 642 (2010).
46. A. Kikhney, Ph.D. dissertation, University of Hamburg, 2010.
47. P. V. Konarev *et al.*, J. Appl Cryst. **36**, 1277 (2003).
48. M. Petoukhov and D. Svergun, Intl. J. Biochemistry & Cell Biology, **45,** 429 (2013).
49. S. Arnis and K. P. Hofmann, Proc. Natl. Acad. Sci. U.S.A. **90**, 7849 (1993).
50. S. Magazu and F. Migliardo, *Dynamics of Biological Macromolecules by Neutron Scattering*, (Bentham Science, Messina, Italy, 2011), pp. 4-8.
51. E. Mamontov, S. O. Diallo, and N. H. Jalarvo, *Oakridge National Laboratory: (Basis) Backscattering Spectrometer*, WWW Document, (http://neutrons.ornl.gov/basis/).
52. X. Q. Chu *et al*., J. Phys. Chem. B **116**, 9917−9921 (2012)
53. X. Q. Chu *et al.*, J. Phys. Chem. Lett. **4**, 936−942 (2013).

ABSTRACT

THE INVESTIGATION OF THE MOLECULAR MECHANISM OF RHODOPSIN ACTIVATION BY SMALL ANGLE NEUTRON SCATTERING AND SMALL ANGLE X-RAY SCATTERING TECHNIQUES

by

KURT WILLIAM VAN DELINDER

December 2015

Advisor: Dr. Xiang-Qiang (Rosie) Chu

Major: Physics

Degree: Master of Science

Rhodopsin is a visual pigment found within the rod photoreceptor cells of the retina. It is a visual protein found within human beings and commonly shared amongst other vertebrate species. The major pigment protein is responsible for converting photons into chemical signals, which stimulates biological processes in the nervous system, and this allows the ability to then sense light [4].

The process of how rhodopsin is activated is believed to be understood with the introduction of a time ordered sequence of intermediate states. However, there are still major gaps and inconsistencies regarding the large-scale conformational changes that follow photo-activation.

The purpose of our experimental research is to use small angle neutron and x-ray scattering techniques to illuminate the structural changes and dynamics of rhodopsin that lead to the activation of the photoreceptor, and thus triggering of the amplified visual response.

AUTOBIOGRAPHICAL STATEMENT

Born in Windsor, Ontario in 1986, Kurt has always had a fond interest in both the physical and health care sciences. As a late teenager, he studied and found role models in the great innovative works of Thomas Edison, Henry Ford and Nikola Tesla. Inspired by their innovative footsteps, Kurt too wanted a niche where he could be given the opportunity to invent and develop new technologies that would also make a significant impact on society. Health care seemed to be the ideal science for such a feat to be achievable. To be even more specific, diagnostic health care. It was then that Kurt found his path in life and future field in which he would pursue as a professional career, the field of Medical Physics.

In 2006, Kurt came up with an academic plan. He would enroll in a B.Sc program in Radiation Therapy, get a M.Sc in Physics and then hopefully get accepted into Medical Physics and complete a Ph.D.

In the fall of 2007, Kurt first started the program Radiation Therapy at Wayne State University. Throughout the four year program, Kurt received high honours and graduated top of his class as summa cum laude. During the program, Kurt was also recognized and placed on the deans honour list for his superb grade point average of 3.72.

In the fall of 2012, Kurt began what would be his first master of science program in general physics also at Wayne State University. Two years later, a completion of the class coursework was finished and is currently in the process of graduating which will take place in the fall of 2014.

In the early months of spring 2014, Kurt received his acceptance letter from the University of Wayne State, Department of Medicine that he was accepted for fall enrollment into the medical physics graduate program.